

POLITECNICO DI TORINO
Repository ISTITUZIONALE

Development and application of a method for characterizing mixture formation in a port-injection natural gas engine

Original

Development and application of a method for characterizing mixture formation in a port-injection natural gas engine / Baratta, Mirko; Misul, Daniela; Xu, Jiajie. - In: ENERGY CONVERSION AND MANAGEMENT. - ISSN 0196-8904. - STAMPA. - 227:(2021), p. 113595. [10.1016/j.enconman.2020.113595]

Availability:

This version is available at: 11583/2850915 since: 2020-11-03T11:38:25Z

Publisher:

Elsevier

Published

DOI:10.1016/j.enconman.2020.113595

Terms of use:

This article is made available under terms and conditions as specified in the corresponding bibliographic description in the repository

Publisher copyright

Elsevier postprint/Author's Accepted Manuscript

© 2021. This manuscript version is made available under the CC-BY-NC-ND 4.0 license

<http://creativecommons.org/licenses/by-nc-nd/4.0/>. The final authenticated version is available online at:

<http://dx.doi.org/10.1016/j.enconman.2020.113595>

(Article begins on next page)

1 **Development and Application of a Method for Characterizing Mixture**
2 **Formation in a Port-Injection Natural Gas Engine**

3
4 Mirko Baratta, Daniela Misul, Jiajie Xu

5 Energy Department, Politecnico di Torino - Italy

6
7 **Abstract**

8 Natural gas has been identified as one of the most promising alternative fuels. Port injection of natural gas,
9 due to its advantages of costs, manufacturing complexity and mixture homogeneity, is relevant to the current
10 and future engine development. The present work aims to provide a comprehensive characterization of gas
11 fuel injection and mixing process, by developing a modeling method for the injector and the engine as a whole
12 serving as a diagnostic tool for further expounding on the basis of experimental results. The injector is
13 modeled by the source cell approach that allows for cost-efficient and physics-consistent description of the
14 underexpanded gas jet, by which a set of fuel injection timings is investigated and then compared with a
15 conventional premixed case. Two mechanisms peculiar to gas port injection are characterized, being firstly the
16 two-stage mixing process that involves immediate induction of the residual fuel from the previous engine
17 cycle and delayed induction of the fuel injected in the current cycle, and secondly the limited fuel penetration
18 speed along the intake ports with associated delay of charge induction. Additional information on volumetric
19 efficiency, mixture quality, coherent flow motion and turbulence level is highlighted. It is concluded that the
20 otherwise intuitive correlation between injection timing and mixture homogeneity for port injection is
21 complicated by those two mechanisms, and, depending on specific engine design and operating point,
22 differences resulted from modeling the engine operation with fuel injection and with premixed charge may
23 prove combustion-significant. The method and the underlying mechanisms found herein are equally
24 applicable to other combustion systems involving port injection of gaseous fuels.

25
26 **Keywords**

27 Natural gas (CNG), Spark-ignition (SI) engine, gas fuel injection, computational fluid dynamics (CFD)

28
29 **1 Introduction**

30 To reconcile the dilemma between the rising demand for the freedom of human mobility and the imperative
31 to mitigate the detrimental environmental impacts caused by such energy conversion services has emerged to
32 motivate decade-long endeavors of research and development in the global transport sector, and will most
33 likely continue to do even more so for the decades to come. This is particularly true for the automotive
34 industry, being a fundamental pillar and the most diffused and diversified element of the modern mobility
35 system, and playing a key role in the economic activity and social connectivity. The ever-accelerating increase
36 in the number of automobiles meanwhile implies great relevance, responsibility, and potential of the
37 automotive industry to tackle the accompanying natural environment deterioration and resource depletion on a
38 broad and significant scale. In particular, internal combustion (IC) engines, which are projected to continue to

39 serve as the dominant technical solution to modern transportation in the foreseeable future [1], must face the
40 challenges with respect to anthropogenic CO₂-induced climate change [2], air pollution [3], and energy
41 sustainability and security [4].

42 The enormous number and ubiquitous usage connected with road transport dictates its multifaceted nature
43 and hence defies the feasibility of pinpointing any monolithic solution. Adopting alternative fuels is a viable
44 approach [5], for their favorable combustion and emission characteristics [6]. . Natural gas has been identified
45 as one of the most promising candidates [7], mainly owing to its clean combustion and the contribution of its
46 antiknock quality to spark-ignition (SI) engine efficiency improvement [8]. Natural gas is an admixture of
47 various gaseous species among which methane (CH₄) is the primary and characterizing constituent. The
48 peculiar physicochemical properties of CH₄, pertaining to the methods for combustible mixture preparation,
49 combustion, and resultant emission formation, make natural gas a major cleaner alternative to conventional
50 liquid fossil fuels [9], promoting extensive discussion on its applicability to SI engines [10] and heavy-duty
51 vehicles [11]. Chemically, methane has the highest hydrogen-to-carbon ratio among all stable hydrocarbons,
52 substantially lowering its fuel carbon intensity. The simple composition also results in a relatively simple
53 combustion chemistry system that suppresses the formation of soot and other complicated intermediate
54 compounds. In addition, the stable and compact tetrahedral molecular structure, with resultant low reactivity,
55 prolongs the ignition delay for CH₄ than other hydrocarbon fuels at elevated pressures and temperatures
56 [12] and over a broad range [13]. Therefore, the combustion regime of methane under typical engine
57 conditions is predominantly the propagating conduction-diffusion-controlled flames rather than the ignition-
58 delay-gradient-driven autoignition, granting CH₄ strong resistance to knocking. As a result, natural gas fueling,
59 with a proper combination of higher compression ratio (CR), higher intake boost and downsizing beyond the
60 typical limits of gasoline engines [14], is a key enabler to increase thermal efficiency and specific power, and
61 fuel economy. Moreover, the gaseous state gives natural gas the inherent advantages of obviating atomization
62 and vaporization, thus avoiding wall wetting and the formation of fuel-rich pockets. Natural gas is also an
63 economic fuel owing to its abundant conventional and unconventional resources [15], and can thus reduce
64 dependency of transport on crude oil and mitigate oil depletion by transport.

65 The gaseous state nevertheless is problematic for practical fuel applications. The density and viscosity of
66 compressed natural gas (CNG), drastically lower than liquid fuels, imposes stringent requirements on injection
67 pressure, injector volume flow rate [16] as well as on manufacturing features such as sealing and lubrication
68 [17]. In this regard, the wide windows allowable for air-fuel mixing in port injection (PI) system, which
69 significantly reduce manufacturing complexity and costs, along with its superior capacity to guarantee mixture
70 homogeneity [18], make PI CNG engine a commercially and technically appealing option to incorporate
71 natural gas into transport fuel portfolio. As a consequence, PI engines are dominant in the current CNG-
72 vehicle market.

73 Gasoline-CNG bi-fuel vehicles, especially taxis, have firstly and long witnessed vast popularity. In fact, the
74 size of the global CNG vehicle fleet has grown by an order of magnitude over the last decade [19], and most
75 of the engines are retrofitted from gasoline ones with CNG PI [20]. Such enduring popularity has attracted
76 continuing researches on, for instance, the modeling of performance and emissions [21], driving-cycle bench
77 tests [22], and real-world emission measurement [23] of bi-fuel PI CNG engines and vehicles, which
78 substantiated their economically-friendly, environmental benefits.

79 The inherent compatibility and potential of CNG in stoichiometric-mixture spark-ignition (SI) combustion
80 system, along with the technological applicability of gas PI system that operates at low pressure (typically

$\leq 1 \text{ MPa}$), has encouraged extensive researches to date on dedicated PISI CNG engines with CNG-specific optimization. Load-dependent specific CO_2 emission reduction by 25–45% was experimentally and theoretically revealed with a gasoline-converted PISI CNG engine optimized in terms of CR, downsizing, exhaust gas recirculation (EGR) rate, and spark timings [24]. In addition, PISI CNG vehicles, thanks to the low-carbon-intensity fuel, were found to produce comparable [25] or less total greenhouse gas emissions in comparison with their diesel counterparts [26], albeit the latter being more thermally efficient. To retain the NO_x emission advantages of CH_4 combustion when CR is typically increased, the mechanism of individual EGR components was experimentally detailed in a PISI CNG engine for control purposes [27]. Test-cycle measurements demonstrated that vehicles powered by PISI CNG engines resulted in lower tailpipe particulate emissions than particulate filter-equipped diesel ones [28]. As a result of the immediately obtainable emission benefits, an important share of dedicated PISI CNG fleet is accounted for by heavy-duty applications, especially the captive vehicles in urban areas. In fact, diesel engines, traditionally predominant in this field, can be efficiently converted to PI CNG by replacing the diesel injector with a spark plug and by adding a port injector. To this end, an empirical and numerical model-based optimization method was developed for converting diesel into PISI CNG engines [29], and the combustion characteristics of natural gas inside a diesel-derived PISI optical engine was observed to assess the influences of typical diesel combustion chamber on flame propagation [30]. Meanwhile a growing number of specifically optimized PISI CNG engines are being introduced into the market for the readily available reduction in emissions and costs [11]. Dedicated PISI CNG engines were also evaluated for small-displacement constant-speed applications such as stationary generator [31] and decentralized cogeneration plant [32], wherein simplification of the injection system and high charge homogeneity are preferable properties. For the same reason, the injection strategy and resultant mixing process inside a PISI side-ported rotary CNG engine, intended as a range extender for hybrid electric vehicles, were numerically studied [33]. The potential of Miller cycle through increased geometric CR and late intake valve timing for thermal efficiency improvement in a PISI CNG engine was explored with positive results [34].

In addition to the direct application in CNG engines, CNG PI has been extensively involved in a variety of alternative combustion concepts. Given the physical similarity of CH_4 to hydrogen with even lighter molecules, the benefits of hydrogen-enriched CNG (HCNG) in terms of flame stabilization and further reduction in fuel carbon content were usually exploited by PI, since the technical difficulties in manufacturing CNG direct injector apply more to HCNG. HCNG PI with solenoid injector was therefore adopted in both experimental single-cylinder study [35] and one-dimensional modeling [36]. The emission benefits of CNG are conveniently incorporated with diesel-like efficiency by dual-fuel, wherein CNG as the main fuel is commonly delivered by PI method to form a premixed charge for which pilot injection of a high-cetane fuel, typically diesel, provides the ignition energy. While researches were usually focused on diesel pilot injection through pre-chamber [37] or multiple injection [38], the combustion process was experimentally shown to be influenced by CNG PI timing as well [39]. Another dual-fuel concept relies on the SI combustion of a fuel blend of gasoline and CNG in order to overcome the volumetric efficiency losses of PISI CNG engines through the synergy between a clean high-octane fuel and a high-energy-density liquid fuel. In this case, the fuel blends were realized by the concomitant injection, by means of either two port injectors [40] or the combination of a gas port injector and a gasoline direct injector [41], generally resulting in improved engine efficiency and emissions with little sacrifice of power output. Moreover, gas PI has been widely applied in combustion systems operated on other gaseous fuels such as biogas [42], hydrogen [43], and DME [44].

Therefore, characterizing PI of natural gas, or of gaseous fuels in general, is highly relevant to the current as well as future development of IC engines. PI is traditionally implemented in gasoline engines wherein the liquid fuel is rapidly injected towards the intake valves during a small fraction of the intake stroke, and adequate mixture homogeneity is normally guaranteed. However, as a consequence of largely reduced density and sonic-limited velocity at injector nozzle, the limited fuel flow rate and prolonged injection duration may result in the mixing characteristics of gas PI distinguishable from liquid PI. In fact, perceivable effects of mixture quality variation attributable to the PI operation were observed. The indicated mean effective pressure (IMEP) data were statistically analyzed to examine the dynamics of cyclic combustion instabilities in a PISI CNG engine, and injection timing was verified to influence combustion stability due to different mixture stratification inside the combustion chamber [45]. A similar study on combustion cycle-to-cycle variation (CCV) in a large-bore PISI CNG engine showed that the CCV, as an indicator of mixture quality, was affected by the port injector elbow types and injection duration as the fuel was delivered into the intake manifold behind the valves [46]. It was also experimentally shown that PI timing had a significant influence on the premixed combustion process in a dual-fuel engine, and was a potential factor for performance optimization [39]. Moreover, varying the gas injection parameters is in fact a common practice for PISI CNG engine calibration which affects optimization objectives such as fuel consumption and emissions. Accordingly, as gaseous fuels are becoming increasingly popular in engine applications and mixture quality is a well-known factor determining the combustion process, investigation into PI and mixture formation processes peculiar to gaseous fuels is necessitated.

To understand the behaviors of gas PI, the gas jet emitted from a production port injector was examined in detail by means of schlieren imaging whereby both free and impinging natural gas jets were visualized so as to represent realistic PI conditions [47]. The study was focused on the assessment of the axial and radial penetration as well as the overall targeting profile of the gaseous fuel jet. A similar optical observation on jet development was performed for a single-hole nozzle injector, presenting the correlation of pressure with tip penetration and mass flow rate respectively [16]. Furthermore, in view of the underexpanded nature of practical fuel injection, the effects of nearfield shock structure on farfield jet evolution and injection parameters were analyzed with various pressure ratios and nozzle diameters, wherein the promoted spatial distribution and turbulent mixing in the shock-dense nearfield were highlighted [48]. It is agreed among those studies that the injection characteristics of gaseous fuel differ from liquids, and supposing that gas PI exhibit peculiar mixing process meriting detailed investigation is plausible. Meanwhile, experimental and numerical studies of CNG engines with port-injected fuel usually assume homogeneous mixtures [49], thus tending to rule out variations potentially attributable to PI operation. To ascertain its influences or lack thereof, the process and underlying mechanisms of injection and mixture formation inside intake manifold and combustion chamber resulting from gas PI, apart from studying the gas jet itself, has to be understood. However, in-detail characterizing methods and discussions in this regard have been scarcely documented in literature. Therefore, the present work aims to present a method for characterizing the gas injection and mixture formation for engines equipped with gas PI.

For investigating experimentally reported influences of gas PI on engine operation, numerically modeling the gaseous fuel injection and air-fuel mixing processes by means of computational fluid dynamics (CFD) is an effective way. CFD modeling allows the complex air flows and its interaction with high-velocity injected fuel to be revealed in three-dimensional details, and is useful for obtaining flowfield properties that are not readily accessible by experimental means. In the present work, the characterization of CNG PI consists in firstly modeling the injector with the source cell method and subsequently incorporating the injector model

167 into the full engine model in order to thoroughly understand the entire injection and mixing process. In
168 particular, the source-cell modeling method for the single-hole gas injector is discussed in detail with respect
169 to model implementation and grid density that are specifically tailored for mixture formation study in gas PI
170 engines. An engine calibration is performed beforehand which substantiates the influences of gas PI timing on
171 engine performance and sets the background for further CFD investigation. By then numerically modeling
172 several engine operation cases with gas injection and comparing with a premixed case, the objective is to
173 provide a comprehensive insight into the mixing characteristics peculiar to gas PI through the presented
174 method, characteristics including the major differences from liquid fuel operation, the underlying mechanisms
175 that governs the mixing between injected gaseous fuel and air, and the influences of gas PI on flow parameters
176 to be considered when designing PISI CNG engines or diagnosing their operation.

177

178 **2 Engine configuration**

179 The engine herein investigated is intended as a high-performance urban mobility solution that incorporates
180 the immediate pollutant and CO₂ emission benefits of natural gas fueling in traffic-dense regions. The
181 prototype is a downsized two-cylinder water-cooled PISI CNG engine that is turbocharged with intercooling.
182 The main engine parameters are reported in Table 1. Variable valve actuation (VVA) is implemented to the
183 intake valvetrain, for which the valve timing reported in the table have to be intended as referred to the full
184 load conditions, as well as to a reference lift of 1 mm. Being a dedicated CNG engine, the CR is elevated from
185 the gasoline baseline up to 13:1 by modifying the piston crown, in order to take advantage of the knock-
186 resistance of natural gas. More specifically, the modified piston features a dome whose size has been fitted to
187 the clearance volume, as can be seen in Figure 1a. Figure 1 also shows the geometry of the cylinder head (Fig
188 1b). The optimization of the engine combustion chamber was studied previously by the authors and it was
189 documented in [50]. Since the intake ports featured a moderated tumble intensity, and given the necessity of
190 sustaining the turbulence intensity at partial load, a configuration with masked intake valve was adopted. The
191 mask showed to inhibit the intake flow on the intake side, thus suppressing the reverse tumble flow at low lift.
192 The effect is clearly visible in Figure 2 (data taken from [50]). In fact, despite the advanced valve closure at
193 partial load, the quite high tumble intensity generated during the intake process allowed the same tumble level
194 as the full load case to be obtained. In both cases, the tumble number peak in the compression stroke was
195 around 0.6 (see Figure 2).

196 The engine is designed to be fueled with natural gas with variable composition. In the experimental tests
197 documented in this paper and in [50], the engine was fueled by natural gas taken from the network, and
198 controlled periodically. The average, detailed, composition is reported in Table 2. A Bosch single-hole
199 injector is mounted to the intake port of each cylinder and fed by a high-pressure CNG storage tank along with
200 two pressure regulating valves.

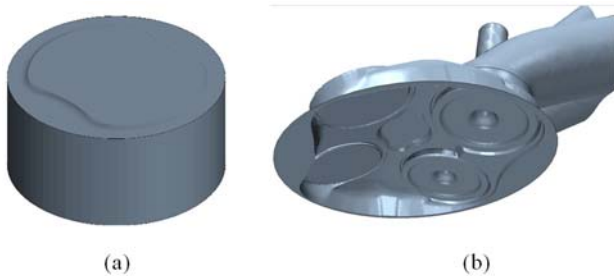
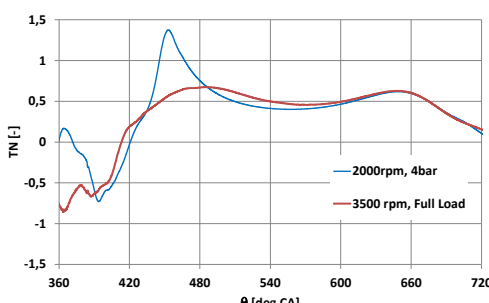


Figure 1 Engine geometry: piston (a), cylinder head (b).**Figure 2** Engine tumble number (from [50]).

	Item	Unit	Value
General Info	Engine	–	SI CNG
	Cylinder	–	Straight twin
	Cylinder head	–	Pent-roof
	Air induction	–	Turbocharge, intercooler
	Turbocharger	–	Wastegate controlled
Crank Train	Bore	mm	72
	Stroke	mm	84
	Connecting rod	mm	128
	Displacement	cm ³	685
	Compression ratio	–	13:1
Valve Train	Valves per cylinder	–	4
	Valve train intake	–	FIAT MultiAir VVA
	Valve train exhaust	–	Fixed cams
Valve timing	IVO	deg CA	368
	IVC	deg CA	Variable - 549÷570 @ Full Load
	EVO	deg CA	145
	EVC	deg CA	360
Fuel Injection	Injection system	–	Multipoint port injection
	Fuel rail pressure	bar	5 – 10 (9 used herein)
	Injector type	–	Single hole
	Hole diameter	mm	1.5

Table 1 natural gas engine specifications

Species	Unit	Value
METANE	%vol	91.8
ETANE	%vol	4.4
PROPANE	%vol	0.9
BUTANE	%vol	0.3
Nitrogen	%vol	2.4

Table 2 Natural gas detailed composition

211 The prototype engine is numerically investigated for diagnostic purposes of providing explanation for the
212 optimum injection timing that has been experimentally identified, and of understanding in detail the influences
213 of injection timing on air-fuel mixing process, fuel distribution, volumetric efficiency and flowfield.

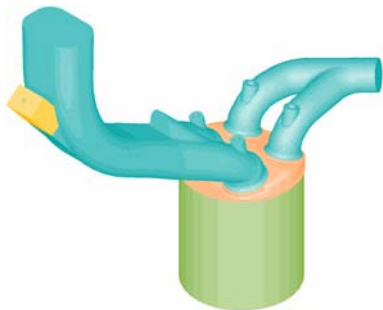
214

215 **3 Model description**

216 Numerical modeling often proves an essential tool for studying the complex internal flow of an engine. The
217 engine cycle including gas injection is modeled in the environment of a three-dimensional finite-volume CFD
218 solver, Star-CD (version 4.20). The model herein presented is an enhanced version of the ones described in a
219 study of tumble flow motion inside a pent-roof engine [51] and in a comparative study of different combustion
220 chamber designs for a PISI CNG engine [50]. While in the previous works combustion was modeled by
221 adopting a homogeneous mixture assumption, in the present work the injection event is described in detail and
222 the mixture stratification characterized. Given that the focus was given to the assessment of the implications
223 of the specific injection simulations, the combustion phase was not simulated in this paper.

224 **3.1 Computational domain**

225 The computational domain encompasses the complete engine geometry including the combustion chamber,
226 intake and exhaust ports that are extended up to the respective collecting manifold (see Figure 3), consisting
227 of hexahedral finite-volume cells. The mesh topology and resolution inside the cylinder and through the
228 valves are the same as in [50]. More specifically, the target cell size in the majority of the volume is imposed
229 at 1 mm, and local refinements are allowed to resolve critical engine geometries. In particular, cells between
230 the valves and corresponding seats are set in the range of 0.2-0.4 mm, considering the high flow velocity
231 during gas exchange phases. Such spatial resolution has been validated in terms of grid sensitivity [50-53],
232 and accepted to be sufficient. Moreover, several parallel layers of gradually coarsened extrusion cells are
233 imposed on the inlet and outlet pressure boundaries to improve accuracy and to attenuate possible boundary-
234 induced perturbation and wave reflection thanks to the increased artificial dissipation.



235 **Figure 3** Overview of the engine geometry and computational
domain (intake on the lefthand side, exhaust on the righthand side)

236 A manually built grid of the injector and housing thereof, with regularly spaced orthogonal hexahedral
237 cells, is integrated into the engine volume (see the yellow grid block in Figure 3), including the injector nozzle
238 in the exact position. The injector location is a typical arrangement for gaseous fuel PI featured in many
239 studies of CNG [45], HCNG [36], and dual-fuel [54] engines. The grid is manually built for good control over
240 mesh quality and spatial resolution both inside and in the proximity of the injector nozzle. A gradual multi-
241 layer transition zone from the highly refined cell sizes to the ~1 mm of the main engine grid is realized.

242 **3.2 Injector modeling**

243 Following the concept introduced in [55], a particular injector model, the source cell method, is applied.
244 Specifically, the injected fuel is introduced into the computational domain as additional source terms in the
245 form of

246 $s_\phi = \dot{m}''' \phi$ (1)

247 where \dot{m}''' is the injected mass flow rate per unit volume, and ϕ a generic flow variable attributed to the
248 injection stream. A proper source term is provided at a selected cluster of cells for each finite-volume equation
249 solved, i.e. the mass flow rate itself ($\phi = 1$) for the continuity-derived pressure equation, the three velocity
250 components for the momentum equations, and the information of temperature and mass fraction for the energy
251 and species transport equations. The prescribed values of the variable ϕ , namely velocity and temperature in
252 this case, are calculated from the upstream condition in the fuel rail according to the location of the selected
253 cluster of source cells relative to the injector nozzle.

254 This method results similarly to a fixed inlet boundary condition but eliminates the necessity of imposing
255 an actual boundary and the corresponding injector inner geometry leading up to the inlet. Nevertheless, it has
256 to be noted that it fundamentally differs from the phenomenological injector models such as notional nozzles
257 with corrected diameters or fictive gas droplets that bypass the underexpansion and associated shock waves.
258 The source cell method introduces the gas flow within the injector nozzle and therefore allows the physical
259 phenomena of an underexpanded jet to be numerically described. The source cell method is presented here
260 with reference to a single-hole injector, however it can be successfully applied also for poppet-valve [55] and
261 multi-hole injectors.

262 **3.3 Numerical strategy**

263 The three-dimensional time-dependent turbulent flow fields are solved by the RANS approach with the
264 RNG $k-\varepsilon$ model. RANS is selected to approximate the mean flowfields for reasonable requirements on the
265 spatial and temporal resolution, especially considering the underexpanded jet that would induce large mean
266 flow gradients and thereby a wide range of turbulence scales. The RNG $k-\varepsilon$ model, accounting for the effects
267 of different scales of turbulent motion, is supposed to improve the prediction of complex flowfield involving
268 swirling and rapid strain changes. RANS with RNG $k-\varepsilon$ model has been commonly applied and validated for
269 reacting and non-reacting engine flows [33,56] as well as specifically for underexpanded jets issuing into
270 quiescent gaseous medium in constant-volume chambers [48,] and for gas fuel injection in engines [57]. It has
271 also been pointed, by a specialized study of numerical settings for simulating underexpanded gas jet [58] as
272 well as by CFD modeling of gas injection into constant-volume chamber [59] and into representative engine
273 geometries [60], out that the various turbulence model variants within the $k-\varepsilon$ family have limited influences
274 on the predicted jet structure.

275 An experimentally calibrated model using the system-level simulation tool, GT-Power, provides crank
276 angle-resolved pressure profiles at the intake and exhaust manifolds that are used for boundary conditions at
277 the same positions in the three-dimensional CFD model. Likewise, pressure and temperature profiles inside
278 the combustion chamber are utilized to initialize thermodynamic state. In particular, the start of simulation is
279 set at 90 crank angle degree (degCA) before exhaust valve opening (EVO), and the initial condition is
280 calculated from a hypothetical polytropic expansion such that the in-cylinder pressure and temperature at
281 EVO are the same as those in the real expansion stroke likely with ongoing combustion. This initialization
282 strategy is crucial to the imposition of a correct velocity field inside the combustion chamber. Due to the large
283 pressure difference, the blowdown in conjunction with the asymmetric exhaust ports (see Figure 3) leads to a

significantly different flowfield than an otherwise symmetric piston-driven one according to preliminary tests. Moreover, concerning the need of getting rid of the influence of the initial conditions, several studies in the literature pointed out the opportunity of simulating multiple cycles. In [61] it was pointed out that in specific conditions it is not possible to reach a stable cycle-to-cycle evolution, and in such cases an ensemble average over the 2nd to the n-th simulated cycles was recommended. This finding was also confirmed in [62], even though it was found that, depending on the mesh size and the engine characteristics, the presence of numerical viscosity can damp the numerical perturbations. With reference to the model used in this paper, a few considerations are anyhow necessary. First, since the combustion phase is not simulated, the expected cycle-to-cycle variation is greatly reduced. Second, from the point of view of mixture stratification, the cyclic variation of turbulence-related quantities has a negligible effect with respect to the fuel-concentration initialization, as it will be discussed in Section 4.3. Third, the model including the detailed simulation of the compressible fuel jet is really CPU-demanding and a compromise between simulation accuracy and calculation time is advisable. According to the preliminary tests carried out by the authors, the simulation of the crank angle interval between 90 deg before EVO and spark timing represented the best compromise for the purpose of the present paper.

The RANS equations are supplemented with the ideal gas model. All geometrical boundaries are treated as adiabatic walls with standard algebraic wall functions. The choice is motivated by the fact that, since combustion is not simulated in the work as already mentioned, the temperature variation is not big enough for meaningful heat transfer to occur. Convective fluxes are approximated by the second-order MARS (monotone advection and reconstruction scheme). The thus computed cell-face centered variables are also used to approximate the diffusive terms. The MARS scheme of second-order accuracy is preferred for the spatial discretization of the momentum equations over the first-order upwinding scheme so as to avoid excessive numerical dissipation of the large gradients associated with the fuel injection. The second-order accurate central differencing (CD) scheme is instead applied to the continuity equation. The time marching procedure is handled by an implicit scheme of a formal accuracy between the first and second order. The velocity-pressure coupling in the momentum equations is solved by the predictor-corrector-based PISO (pressure-implicit with splitting of operators) algorithm.

4 Results and discussion

For the reason of clarity, pure CH₄ is hereinafter used as the surrogate fuel for natural gas. The convention of engine crank angle is such that the firing top dead center (TDC) is at 0 degCA, or periodically 720 degCA, and accordingly 360 degCA corresponds to the valve-overlapping TDC, which is consistently used throughout the present work.

4.1 Injector modeling

This section presents the different implementations and grid dependence study of the source cell method and hence a generalization thereof for the purpose of numerically characterizing gas fuel injection.

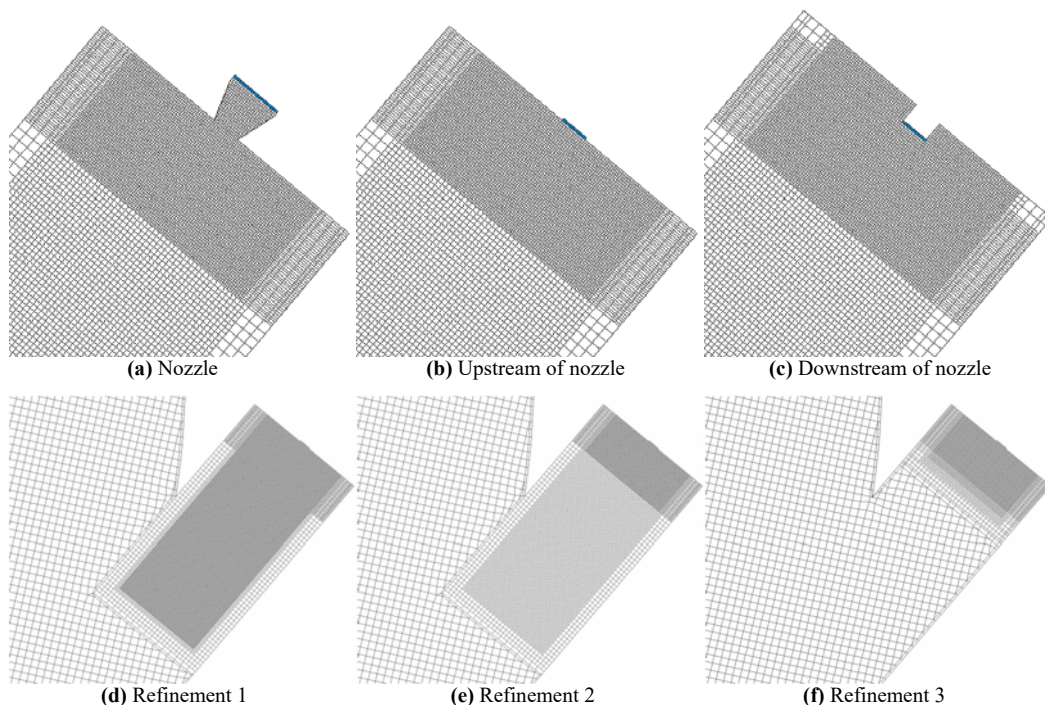
The effects of location of the source cell cluster, wherein the source terms in Equation (1) are introduced, are inspected with three locations relative to the inner injector geometry (see the blue-colored cells in Figure 4). The near-tip flow passage of the injector is conceptually a convergent nozzle with the exit being the critical section. A conical nozzle with ~30° convergent angle is implemented, called case "nozzle" hereinafter, and the

324 source cells are located at a distance from the critical section. The velocity (in terms of Mach number) and
 325 temperature for the source cells are calculated from [63]:

$$326 \quad \frac{A}{A_r} = \frac{1}{M} \left(\frac{1 + \frac{\gamma - 1}{2} M^2}{\frac{\gamma + 1}{2}} \right)^{\frac{\gamma + 1}{2(\gamma - 1)}} \quad (2)$$

$$327 \quad \frac{T_0}{T} = 1 + \frac{\gamma - 1}{2} M^2 \quad (3)$$

328 where A is the known cross-section area where the source cells are located, A_r the critical-section area of the
 329 injector nozzle, T_0 the stagnation temperature in the fuel rail (which is kept almost constant in the normal
 330 engine functioning), T the temperature of the source cells, $\gamma = 1.32$ the specific heat ratio for CH₄, and M the
 331 Mach number. In the other two cases, the source cells are directly at the critical section and, since a
 332 geometrical section cannot be represented by finite-volume cells, one case has the source cells immediately
 333 upstream of the critical section, hence called case "upstream of nozzle" hereinafter, and the other case at
 334 immediate downstream, called case "downstream of nozzle". An extrusion of the surrounding grid is built in
 335 the last case. For these two cases, the critical temperature is calculated according to Equation (3) inserting
 336 $M = 1$ and the velocity corresponds to the local speed of sound since the injector is always choked. The aim
 337 is to examine if different flow structures and mixing behaviors would result from the two source cell locations
 338 that should have both otherwise been located at the exact critical section if not for the limiting finite-volume
 339 discretization. Mass flow rate per volume, \dot{m}''' , for the source term is derived from the same injection rate.
 340 Case upstream and downstream of nozzle share the same per-volume value, different from case nozzle as it
 341 has a larger source cell volume.



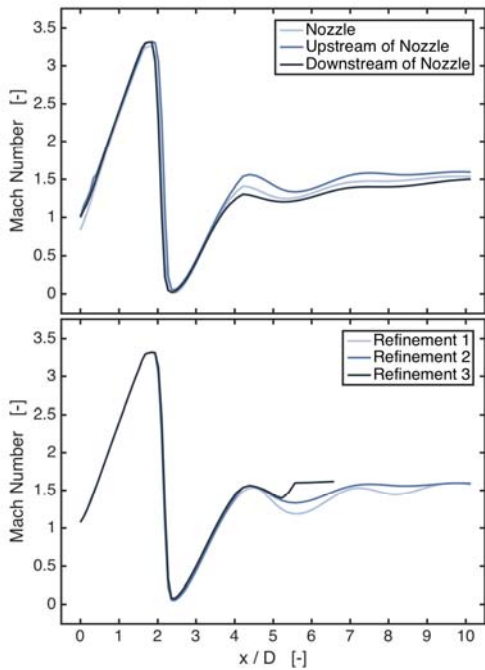
342 **Figure 4** Modelling of the port-fuel injector with different source cell locations (upper row) and local grid refinement levels (lower row)

343 The grid dependence deals with the spatial resolution in the proximate region downstream of the injector
 344 exit, relative to the cell size in the nozzle. The number of cells, and thereby the cell size, used to resolve the
 345 nozzle is instead fixed and the validity is discussed in the next section. Specifically, 12 cells across the 1.5

346 mm nozzle diameter, resulting in 0.125 mm cell size, are placed inside and in the immediate downstream of
 347 the nozzle. A level-wise transition (multiplied by 2) is realized towards the bulk engine grid. Accordingly,
 348 three distinct refinement zones with cell sizes of 0.125, 0.25 and 0.5 mm are imposed for a gradual transition
 349 and conformal node connection.

350 The grid dependence study is to examine the necessary extension of each refinement zone for an acceptable
 351 description of the underexpanded injection and mixing process, acceptable in the sense of a tradeoff between
 352 result fidelity and computational overhead. A refined grid is expectedly requested by the shock wave-
 353 containing, albeit inviscid and non-mixing, core flow and by the large shear in the peripheral mixing layer.
 354 Three refinement cases are conceived for this purpose (see Figure 4). In common, the finest 0.125 mm zone
 355 covers the initial range, designated by x/D (the distance x from the nozzle exit normalized by the nozzle
 356 diameter D) ≤ 4 , essential to capturing the high underexpansion and the first shock cell. In case refinement 1,
 357 this finest cell zone is further extended up to $x/D = 20$, whereas in case refinement 2 that same range is
 358 covered by the next refinement level of 0.25 mm. In case refinement 3, a rapid transition of 4 layers for each
 359 remaining refinement level after the initial range is implemented that in total spans the range of $x/D \leq 6$ to
 360 which the bulk engine grid is connected. Case refinement 2 in fact coincides with the abovementioned case
 361 upstream of nozzle.

362 The nearfield shock structures of the fully developed jets resulted from the source cell-modeled injector are
 363 quantitatively compared in Figure 5, wherein the Mach numbers along the injector centerline are presented
 364 against the normalized distance x/D .



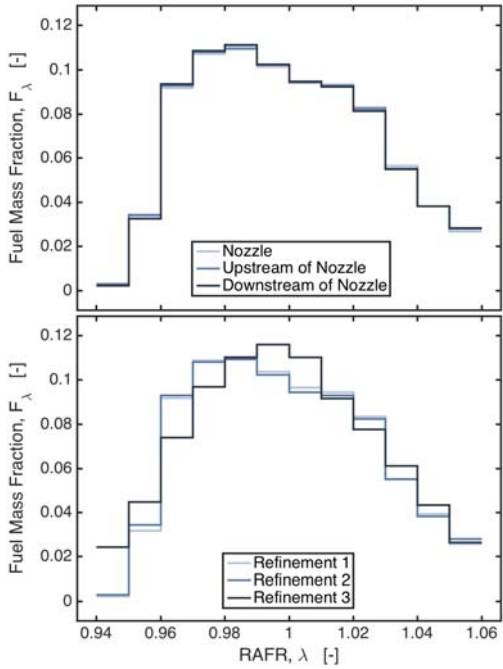
365 **Figure 5** Mach number of the fully developed jet along the
 injector centerline

366 With a partial inclusion of the inner flow passage, case nozzle initially features a subsonic speed, indicating
 367 that the source terms calculated from isentropic nozzle theory are an underestimation. This behavior is
 368 attributable to the decrease in discharge coefficient caused by the curvature of upstream converging
 369 streamlines and to the transition in the boundary layer caused by viscous effects [64]. The subcritical flow
 370 reaccelerates to supersonic state shortly downstream. Eventually all three cases of source cell location attain

371 the same first shock structure at $x/D \approx 2$. Differences in Mach number appear from $x/D = 4$ onwards. The
372 discrepancies are nonetheless considered less of a concern since, firstly, the Mach disk and the first shock cell,
373 typically dominant in highly underexpanded jets, are identically predicted. Secondly, magnitudes of the
374 differences present in the subsequent minor shock structures are insignificant.

375 As to the grid dependence, the three cases describe the first shock cell in exactly the same way as a result of
376 the commonly imposed initial refinement zone up to $x/D = 4$. Accordingly, the numerical model is
377 physically plausible in that the first shock cell by its supersonic nature is supposed to be indeed unaffected by
378 downstream grid structures whose effects are blocked by shock waves. Furthermore, the limited refinement
379 zone in case refinement 3 proves insufficient for capturing the minor shock cells as the periodicity is lost. The
380 multiple minor shock structures in the potential core are described in both case refinement 1 and 2, with the
381 latter case featuring a lower amplitude due to its doubled cell size than the former case. The diminishing
382 wavelengths are nonetheless the same, and the discrepancies in wave amplitude are very small. The periodic
383 structures downstream of the Mach disk are expected. The pressure ratio herein for the fuel injection lies on
384 the ambiguous borderline of the transition from highly to very highly underexpanded jets, ambiguous in that
385 the criteria have been set on an empirical basis and the transition itself is more gradual than abrupt [64].
386 Consequently, the underexpanded jet is predominantly but not exclusively characterized by the first shock
387 cell.

388 It is worth clarifying that the objective of the injector modeling is to identify a suitable method for
389 analyzing mixture formation inside the combustion chamber, and therefore a highly accurate description of the
390 complex shock waves is beyond the scope. From the perspective of engine operation, the mixture at the spark
391 event is of the utmost interest which fundamentally affects the combustion process in terms of ignitability,
392 stability, flame propagation rate and pollutant formation. To this end, the probability distribution of the in-
393 cylinder fuel mass with respect to relative air-to-fuel ratio (RAFR, or lambda λ) at the spark event in the range
394 $\lambda = 1 \pm 0.06$ is presented in Figure 6 as a representation of the final mixture homogeneity. The probability
395 distribution is derived from statistically analyzing the instantaneous CH₄ mass fraction in all the finite-volume
396 cells.



397 **Figure 6** In-cylinder fuel mass distribution at spark event

398 Consistent with the previous observations in Figure 5, the excessive numerical dissipation of case
 399 refinement 3 overestimates the jet spreading and mixing rate, and this effect of artificially enhanced diffusion
 400 is carried over into the combustion chamber to result in a more homogeneous final mixture than the other
 401 cases (appearing as a narrower distribution around $\lambda = 1$). In the meanwhile, extremely subtle differences in
 402 the final mixture distribution result from the three cases with different source cell locations as well as from
 403 case refinement 1 and 2, further confirming that the small discrepancies in describing the minor shock cells
 404 posterior to the dominant Mach disk have insignificant impact on the mixing process inside the combustion
 405 chamber. Case refinement 1 and 2 are therefore considered equivalent in terms of mixing process, indicating
 406 the achievement of grid independence. In fact, as a result of the extensive highly-refined zones, the injector
 407 grid alone in case refinement 1 contains ~ 1.9 million cells, comparable with the ~ 2.1 million cells of the
 408 remaining engine grid that is already a refined mesh by RANS standards. Case refinement 1 hence incurs
 409 substantial computational overhead with largely diminishing improvement in predicting the mixing process,
 410 especially towards the combustion onset.

411 It is concluded that, with the source cell modeling method, the first shock cell, Mach disk and mixture
 412 formation are independent of whether the nozzle flow is simulated from upstream or directly at the critical
 413 section, as long as an initial zone with the cell size identical to that across the nozzle covers the first shock cell
 414 and a refinement zone of sufficient resolution and extension covers the rest of the potential core.

415 **4.2 Model validation**

416 The model validation presented here focuses on the prediction of the compressible, underexpanded fuel jet,
 417 since the overall engine model is essentially the same as in [50] and was extensively validated there. In
 418 addition, the experience done in previous works on the simulation of underexpanded jets was taken as
 419 reference [52, 55, 58]. Based on the universal similitude of circular nozzle flowfield, resolving the injector
 420 orifice with 12 cells across its diameter is considered appropriate by referring to pertinent grid dependence
 421 studies on gas injection. Specifically, it has been verified that from 10 cells upwards the grid sensitivity of

flows near the nozzle is largely reduced [65], and similarly, that using more than 10 cells across the nozzle brings about little effects on jet development, penetration and mixing behaviors [66]. In addition, the combined effects of spatial resolution and discretization schemes were studied in [58], arguing that 20 diameter-wise cells with the first-order upwind scheme were sufficient for a fully grid-independent description of the time-dependent jet evolution and mixing process, whereas equivalent results were attainable with 10 cells and the second-order MARS scheme that also provided a good prediction of the typical underexpanded shock structure. Given 10 cells appearing to be the convergence point, 12 cells are herein imposed for an extra safety margin and considered methodologically validated. Furthermore, pressure ratios involved in all the reference studies were much higher than that in the present work, and theoretically less than 10 cells may already suffice.

Considering that the normal shock is identically captured by all the modeling options above, the predominant shock-relevant Mach disks, specifically the position thereof, are compared with references. In fact, Mach disk position is the only parameter that has been extensively studied with well-documented correlations with pressure ratio [64]. The compressibility-governed flow phenomena in the potential core have long been proven to be primarily dependent on pressure ratio. In this work, the injection pressure p_0 is 9 bar and the ambient pressure p_a inside the intake ports corresponding to the crank angle in Figure 5 is about 0.85 bar (a specific crank angle has to be referred to since the pressure during an engine cycle varies continuously), resulting in $p_0/p_a \approx 10.59$.

An empirical relation based on a collection of experimental measurements was proposed in [67] for the correlation between normalized Mach disk position and pressure ratio, and is reported in Equation (4). Another similar experiment-derived relation, with a slightly different coefficient, as proposed by experiments on free jet in wind tunnel [68] and supported by another study of axisymmetric jet [69] is reported in Equation (5). Both relations imply that the Mach disk position is insensitive to factors other than the pressure ratio. Alternatively, the correlation was formulated as also a weak function of γ through dimensional group analysis [70], reported in Equation (6), so as to consider the thermodynamic effects.

$$2.4 \left(\frac{x_{MD}}{D} \right)^2 = \frac{p_0}{p_a} \quad (4)$$

$$\frac{x_{MD}}{D} = 0.67 \sqrt{\frac{p_0}{p_a}} \quad (5)$$

$$\frac{x_{MD}}{D} = \frac{1}{2} \sqrt{\gamma} \left(\frac{\gamma + 1}{\gamma - 1} \right)^{\frac{1}{4}} \sqrt{\frac{p_0}{p_a}} \quad (6)$$

where x_{MD} is the position of Mach disk along the jet centerline from the exit section. Mach disk positions according to the various relations slightly differ from one another yet no verdict has been finalized, although Equation (4) and (5) have been referred to more often in the literature.

The Mach disk position predicted by the injector model in the present work (see Figure 5) and the values calculated from the correlations above are compared in Table 3. The predicted result closely reproduces the two empirical relations, and is less than 5% lower than the analytical formulation using $\gamma = 1.32$ for CH₄, indicating that the numerical model is reasonably valid. The good agreement additionally implies that the injector modeling by means of source cells is able to produce consistent underexpanded jet structures that are equivalent to the results obtained by the conventional modeling approach using boundary conditions at the

459 upstream nozzle inlet, substantiating the same argument made in [58].

p_0/p_a	x_D/D			
	Present	Equation (4)	Equation (5)	Equation (6)
10.59	2.154	2.100	2.180	2.258
	0	+2.6%	-1.2%	-4.6%

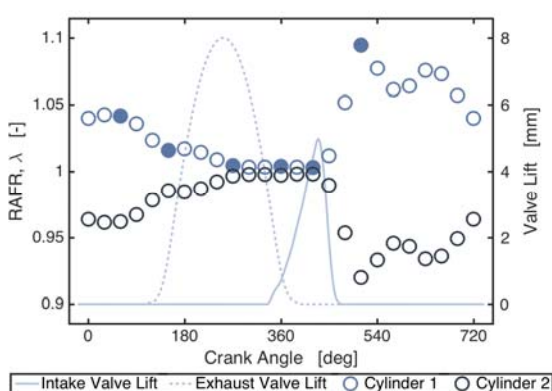
460 **Table 3** Comparison of Mach disk positions

461 In view of the source-cell location sensitivity and grid dependence of the in-cylinder mixture formation
462 process, the injector model with the configuration of case upstream of nozzle and case refinement 2 fits well
463 the scope of the present work, and is hereby used for the detailed diagnostic investigation into the mixing
464 mechanism of PI operation.

465 4.3 Injection timing and mixture formation

466 Experimentally, an injection sweep over the entire 720 degCA engine cycle for the operating point 2000
467 rpm low part load (IMEP = 4 bar) is performed on the prototype engine to investigate the effects of injection
468 timing. This particular operating point is selected for two reasons: first, the close-to-low-end engine speed
469 largely hinders in-cylinder charge motion; and second, the VVA-enabled short intake opening window and
470 small lift, typical of part-load operations, is problematic for charge induction. End of injection (EOI) at 270
471 degCA is identified as the optimum timing according to engine calibration in terms of fuel consumption,
472 hydrocarbon and carbon monoxide (HC and CO) emissions, and mixture homogeneity, with operational
473 abnormalities occurring at other timings.

474 To reveal the underlying mechanisms that elude experimental testing, the injection sweep is reproduced in
475 the previously mentioned GT-Power model. The RAFR distribution between the two cylinders is presented in
476 Figure 7 including all the investigated EOIs at 30-degCA intervals. The VVA-reduced intake valve
477 profile indeed constrains charge induction, as a small fraction of the engine cycle (from ~150 to 420 degCA)
478 is usable for EOI variation to produce an even inter-cylinder fuel distribution. For EOIs outside this range, the
479 symmetric patterns indicate that fuel crossing from one cylinder to the other occurs. Six injection timings (see
480 filled dots in Figure 7) are selected for further CFD analysis, among which the early and late EOIs (60 and
481 510 degCA) are for understanding the fuel crossing and four EOIs within the usable window (150, 270, 360
482 and 420 degCA) for detailed mixture formation mechanisms. More precisely, injection timings are termed
483 relative to the intake valve closing (IVC) for PI engines, and accordingly EOI 510 degCA is the earliest timing
484 and 420degCA the latest.

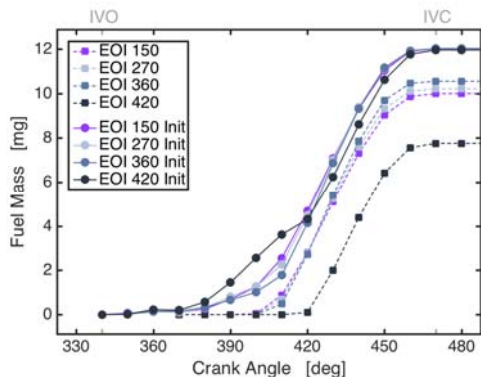


485 **Figure 7** Injection sweep results for different EOI timings (at 30
degCA intervals)

486 Two phenomena are revealed. Firstly, the injected fuel, accumulating in the intake ports for case EOI 60
 487 and 510, is drawn reversely into the intake manifold due to pressure drop caused by the intake phase of the
 488 other cylinder. Therefore, the injection timing cannot be set anywhere throughout the entire 720 degCA range
 489 to fully exploit the hypothetical long mixing time of PI operation. Instead, there exists a threshold for gas-
 490 fueled PI engines, earlier than which fuel crossing is inevitable.

491 The second, more peculiar phenomenon is termed the two-stage mixing process. Fuel injected before IVO
 492 of each engine cycle is in fact partially inducted and burned in the same cycle. And a portion is left in the
 493 intake ports after IVC. Consequently, except for the first cycle of an operating point, the fuel inducted into the
 494 combustion chamber consists of residual fuel from the previous cycle and injected fuel from the current cycle.
 495 From the perspective of numerical simulation, the residual fuel distribution inside the intake ports has to be
 496 considered for flowfield initialization so as to reflect the actual mixing process. It is verified that the residual
 497 fuel distribution of each engine cycle clearly reaches a steady state, for which the two-stage mixing process is
 498 detectable in neither experiments nor system-level simulations.

499 The two-stage mixing process is influenced by injection timing. Figure 8 shows the differences in inducted
 500 fuel mass between simulations with and without initialization of the intake port residual fuel, for the four
 501 investigated EOIs. Two distinct induction stages are identifiable. Initially, due to limited fuel traveling speed
 502 from the injection site to intake valves, induction occurs much later than IVO for cases without residual fuel.
 503 For the other group with initialization, the first empty window is filled by induction of the residual fuel. Such
 504 distinction not only influences the amount of fuel eventually present inside the combustion chamber after
 505 IVC, but, more importantly, implies two mixing stages, i.e. the mixing of initially inducted residual fuel and
 506 the mixing of freshly injected fuel that arrives later.



507 **Figure 8** Cumulative fuel mass present in the combustion
 chamber for different EOI timings

508 Accordingly, injection timing has a two-fold impact on the mixing mechanisms. On the one hand, the
 509 amount of time for the freshly injected fuel to arrive at the intake valves and thereby the amount of fuel
 510 involved in the second mixing stage may vary with injection timing. On the other hand, delayed injection may
 511 result in increased residual fuel that partakes in the first mixing stage of the succeeding engine cycle. The two-
 512 stage fuel induction process of case EOI 270 and 420, as an example, is illustrated in Figure 9 by comparing
 513 the cases with and without residual fuel initialization so as to individualize the first and second stages (as the
 514 figures are for qualitative purposes, colormaps are omitted for simplicity and the scale is kept the same for
 515 all). Figure 9 (a) shows the empty window of intake phase prior to the arrival of injected fuel and the first-
 516 stage induction of residual fuel that in turn depends on the injection timing. Case EOI 420 has higher amount
 517 of residual fuel and correspondingly more fuel is inducted and mixed in the combustion chamber during the
 518 first stage. The fresh fuel reaches the intake valves and the second-stage induction begins subsequently, as

519 shown in Figure 9 (b) and (c). It is observed that the two stages are independent since the cases without
 520 initialization show the same inducted charge flows as cases with initialization. The sole difference is the
 521 preexistent mixture inside the combustion chamber in the latter cases. Furthermore, as shown in Figure 9 (b),
 522 delaying the injection event leads to more fuel flowing through the righthand section of the intake valves than
 523 the lefthand side. As a consequence, pure air may be inducted for the intervening duration between the end of
 524 the first stage and the start of the second. Since the inducted charge, albeit partially premixed inside the intake
 525 ports, remains rich in fuel, the distribution of fuel-rich pockets in the combustion chamber upon IVC is
 526 fundamentally determined by the particular induction sequence of residual fuel, injected fuel and air, if any,
 527 which is evident in case EOI 420.

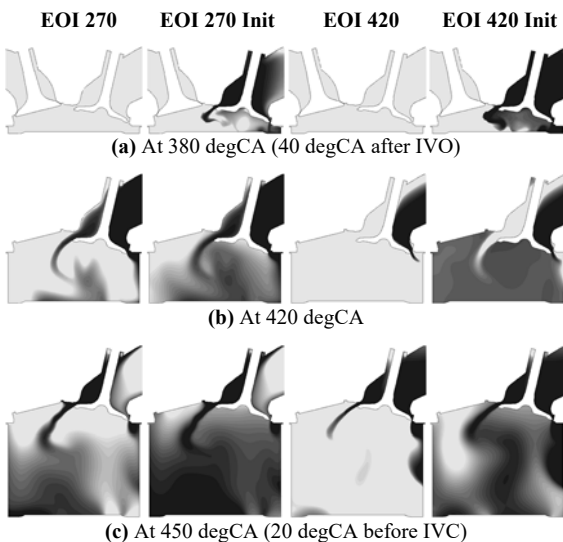


Figure 9 Fuel mass fraction contours during the intake phase with
 and without residual fuel initialization
 Grayscale: darker = higher fuel mass fraction, lighter = lower fuel
 mass fraction

528 In summary, the effect of injection timing on in-cylinder mixture formation is vastly complicated by the
 529 two-stage mixing mechanism, peculiar to PI of gas fuels. This mechanism depends on the total injected fuel
 530 quantity, the proportions thereof inducted in the first and second stages, and the time that the injected fuel
 531 spends traveling from injector to intake valves.
 532

533 The mixing process inside the combustion chamber for different EOIs is presented in Figure 10, statistically
 534 quantified as the coefficient of variation (CoV) in fuel mass fraction across the whole chamber and as the fuel
 535 mass fraction enclosed in the flammable mixture. The flammable mixture is defined as the sum of all finite-
 536 volume cells whose cell-wise RAFR lies between 0.7 and 1.7, the flammability range of natural gas according
 537 to experimental data [71].

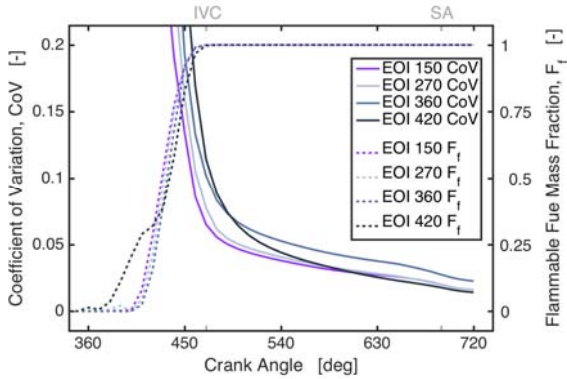


Figure 10 Mixing process inside the combustion chamber for
538 different EOI timings (SA: spark advance)

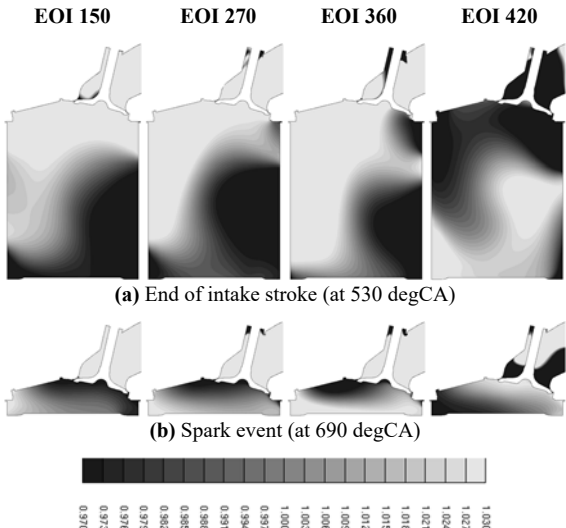
539 The principal mixing process occurs during the intake phase as the CoV decreases most rapidly in that
540 period prior to IVC. Moreover, the flammable mass fraction already reaches unity upon IVC, indicating
541 flammability of the entire mixture regardless of the injection timing. Both observations correspond well to the
542 typical behaviors of PI engines.

543 However, combustion depends further on the homogeneity of the flammable mixture and on detailed fuel
544 distribution at the spark advance which in turn relies on continuous air-fuel mixing during the remaining
545 intake and compression strokes. Mixing rates after IVC for all EOIs are significantly lowered, as a result of
546 low engine speed and coherent charge motion for which the choice of investigated operating point is
547 specifically purposed. Furthermore, the declining rates of individual CoV curves differ among the four cases,
548 and no general trends appear to correlate the differences with EOIs. With the injection 120 degCA later, case
549 EOI 270 exhibits extremely similar mixing rate to case EOI 150, whereas the mixing rate for case EOI 360 is
550 notably lower even though the injection is delayed by a lesser 90 degCA relative to case EOI 270. Case EOI
551 420, despite being the latest injection, features the highest mixing rate.

552 The apparent decoupling between mixing rate and injection timing is in fact found to be the consequence of
553 two counterbalancing effects caused by the same variation in EOI. On the one hand, advancing the injection
554 expectedly promotes air-fuel premixing prior to the intake phase. This trend by nature is monotonic with EOI,
555 and is evidenced by the part of CoV curves before IVC in Figure 10. On the other hand, postponing the
556 injection gives rise to a larger amount of residual fuel to partake in the first-stage mixing of the succeeding
557 cycle. For the same total amount of inducted fuel in each engine cycle, evenly distributing the fuel subtotals
558 between the two mixing stages enhances mixing by increasing the number of local fuel-rich mixing sites. This
559 is particularly obvious for case EOI 420 as the first-stage residual fuel accounts for ~1/3 of the total inducted
560 fuel mass (see Figure 8), explaining its high mixing rate. In addition, as pointed out earlier, largely postponing
561 the injection (EOI close to IVC) introduces an empty window between the end of the first induction stage and
562 the start of the second, during which no fuel but air enters. The intervening air induction also contributes to
563 spreading out fuel-rich pockets and may affect the mixing process.

564 The fuel spatial distributions towards the end of intake stroke are presented in Figure 11 (a) as an example
565 to illustrate the relevance of mixing sites. The two counterbalancing effects of injection timing are such that
566 earlier injections result in broader fuel-rich pockets (due to better out-of-cylinder premixing) but meanwhile
567 the fuel-rich zones are more restricted in space (due to more predominant second-stage induction). For case
568 EOI 360 the splitting of fuel between the two induction stages appears to be insufficient for the marginal first
569 stage to compensate for the less premixed second stage. The mixing rate of case EOI 360 is hence low relative

570 to both the more premixed cases with earlier injection and to the later injection with two comparable fuel-rich
571 zones spread at a distance by intervening air induction.



572 **Figure 11** Fuel mass fraction contours for different EOI timings

573 The particular pattern of fuel distribution determines the subsequent passive mixing process in the
574 compression stroke. Figure 12 presents, at the spark event, the probability distribution of fuel mass with
575 respect to RAFR and fuel mass fraction as a function of deviation η of the local mixture RAFR from the
576 stoichiometric ratio 1, i.e. the mass fraction of fuel enclosed in mixtures whose RAFR is $1 \pm \eta$. Both are
577 statistical metrics indicating mixture homogeneity. The resultant final mixture quality of the most interest is
578 characterized by the same trend as the mixing rate. Case EOI 150 and 270 result in mixtures that are
579 equivalently homogeneous, with the later injection being slightly more so. As a result of low mixing rate, case
580 EOI 360 produces a notably less homogeneous mixture. The mixture from the latest injection, case EOI 420,
581 has the highest homogeneity thanks to its highest mixing rate after the intake phase.

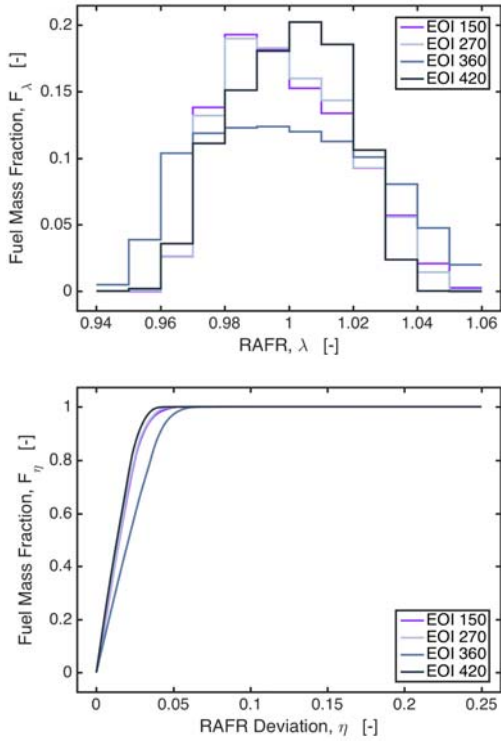


Figure 12 Fuel mass distribution (upper) and fuel mass fraction as a function of RAFR deviation (lower) at the spark event

582

From the perspective of mixture homogeneity, case EOI 420 is supposed to be the best according to the statistical evaluations in Figure 12. The experiments on the prototype engine however pinpoint case EOI 270 to be the optimum timing, which can be justified by the fuel spatial distribution and the cycle-to-cycle variation. It is worth pointing out that the latter depends mostly on the local conditions governing the ignition process, and is not fully predictable by a RANS model. Still, the RANS approach presented in this paper allows the relative effect of injection timing to be described. Despite that the final mixture of case EOI 270 at spark event is statistically less homogeneous to a small extent, its local fuel distribution as shown in Figure 11 (b) favors the flame propagation to the largest extent among all the investigated timings. Case EOI 420, albeit having the most favorable mixing process, results in the exactly opposite fuel distribution. The relatively lean mixture in the upper region is known to adversely impact flame kernel stability and early quasi-laminar flame propagation, whereas the rich mixture near the piston crown may inhibit complete combustion and increase crevice-trapped fuel. Case EOI 360 has similar fuel distribution to case EOI 270 but the homogeneity is less ideal.

596

4.4 Injected fuel traveling

597

The injected fuel, due to the low momentum of gas jet limited by nozzle sonic speed and density, arrives at the intake valves after a perceivable delay. The finite fuel traveling speed plays a crucial role in the two-stage mixing mechanism, since it determines the start of the second-stage induction and the amount of residual fuel for the first stage. To further investigate the fuel traveling inside the intake ports, two test groups are designed with in total five cases. The cases and resultant fuel traveling are presented in Figure 13. Specifically, the previous case EOI 270 and 420 (at 2000 rpm) are retained as references to which three cases at doubled engine speed (4000 rpm) are added. Apart from injection timings and engine speeds, all other engine parameters remain the same. With the same total injected quantity, cases at 4000 rpm have double the

598

599

600

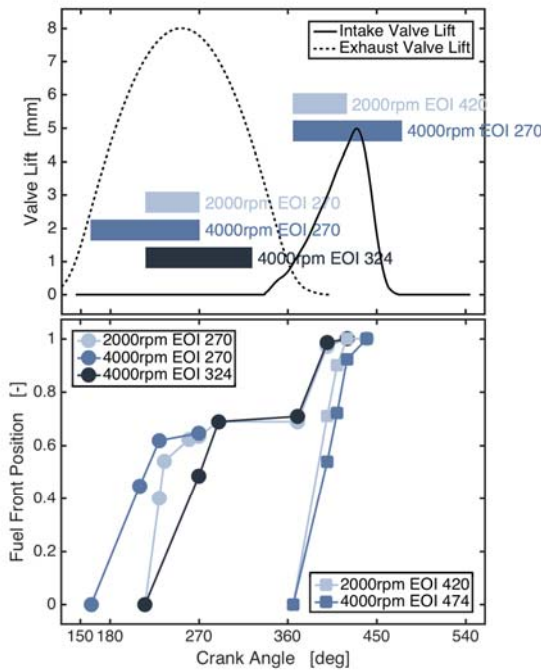
601

602

603

604

605 injection duration in degCA due to doubled engine speed. The fuel front position designates the distance along
 606 the intake port from the injector tip whereat the farthest front of the injected fuel is located, normalized by the
 607 total distance from injection tip to intake valves.



608 **Figure 13** Case setup and results for fuel traveling investigation

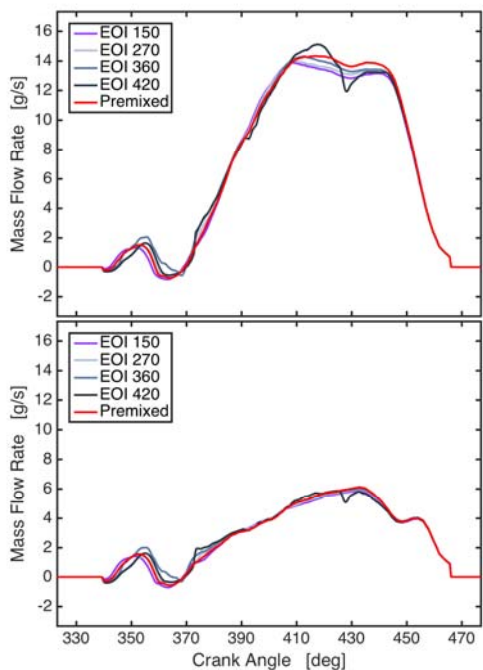
609 In the first group, all the three injection events are finished before IVO, and the two at 4000 rpm have either
 610 the same start of injection (SOI) or EOI as the reference case 2000 rpm EOI 270. As the intake valves remain
 611 closed, the initial fuel penetration is solely propelled by the ongoing injection and thereby scaled with absolute
 612 time instead of degCA. This is evidenced by the equal slopes of the two 4000 rpm cases EOI 270 and 324.
 613 Case 2000 rpm EOI 270 has double the slope that would in fact be the same as the other two cases if
 614 expressed in unit time. Another peculiar feature is that the fuel penetration stalls at the position where the
 615 intake pipe branches into two leading to the intake valves (at approximately the 0.7 position into the intake
 616 ports), likely ascribable to pressure buildup that acts against the incoming fuel flow. The fuel penetration then
 617 resumes upon IVO. This feature of fuel stagnation profoundly influences charge induction and mixing
 618 process. First of all, for a certain injection timing with which the fuel travels exactly to the branching point at
 619 IVO, the expected earlier fuel traveling to intake valves by further advancing the injection would simply be
 620 negated, explaining the reason that the previous case EOI 150 and 270 show almost identical start of the
 621 second-stage induction (see Figure 8) despite a difference of 120 degCA in EOI. Secondly, the early injected
 622 fuel accumulates in the upper segment of intake ports and is therefore prone to fuel crossing. The resumed fuel
 623 penetration, no more energized by injection, assumes the same rate in degCA for all the cases, implying that
 624 the driving force is the piston movement, scaling with degCA instead of time.

625 In the second group, the two injection events occur entirely within the intake phase, and the jet penetration
 626 is consequently under the joined influences of injection and piston movement. The two cases exhibit very
 627 similar slopes as the piston speed scales with degCA, whilst the case at 2000 rpm is slightly but not twice
 628 steeper than the 4000 rpm case indicating the existent but not dominant driving force of injection.
 629 Furthermore, there appears to be not fuel penetration stalling due to the ongoing intake phase. And the
 630 correlation between early injection and early fuel induction is supposed to be straightforward.

631 **4.5 Comparison with premixed charge**

632 Conventionally, most numerical studies on PI engine have been performed with perfectly premixed charge
633 in either intake ports or combustion chamber, presuming unnecessary simulating the injection process. In view
634 of the peculiar mixing mechanisms, a comparative study with a case of homogeneous stoichiometric mixture
635 preset in the intake ports, in addition to the four cases at 2000 rpm in the injection timing study, is carried out.
636 All other engine parameters remain unchanged.

637 The mass flow rates through the intake valves, the variable most fundamental and pertinent to the two-stage
638 mixing mechanism, are presented in Figure 14. The annular opening of the intake valves is conceptually
639 divided into two halves by a plane passing through the centerlines of the two valves. The half section on the
640 exhaust side is responsible for the typical tumble motion in pent-roofed SI engines, and the other half on the
641 intake side facing the adjacent liner admits minor flows (corresponding for instance to the left and right intake
642 flows in Figure 9, respectively). Assuming the same pattern of intake volume flow rate, differences in mass
643 flow rate can be interpreted as variation in local fuel concentration, given that the density of CH₄ is about 0.55
644 of that of air at the same pressure and temperature.



645 **Figure 14** Mass flow rate through exhaust half section (upper)
and intake half section (lower) of intake valves

646 After the initial impulsive inflow and backflow, the first-stage induction begins at 370 degCA with subtle
647 differences in mass flow rate across all the cases, as the residual fuel from the previous cycle has premixed
648 with local air long enough to produce similar concentrations. Corresponding to Figure 8, appreciable
649 differences appear at 410 degCA when the second-stage induction starts for the three earlier cases and at 430
650 degCA for case EOI 420. Due to different injected fuel arrival time, more air is being inducted through the
651 exhaust-side half section for more postponed EOIs, represented by higher mass flow rate. Mass flow rate of
652 the premixed case lies above the three earlier cases but below case EOI 420 wherein pure air is being
653 inducted, indicating that the instantaneous intake flows of the earlier cases are far from being perfectly
654 premixed. This trend continues till the rapid closing phase of the intake valves, except for case EOI 420 whose
655 later started and much less premixed second-stage induction drastically decreases its mass flow rate. In the

meanwhile, the differences in the intake-side half section are milder, especially for the overshoot of case EOI 420 at 410 degCA, as fuel-rich mixture is being more consistently admitted without distinct intervening air induction. This observation substantiates the previous findings in Figure 9. Nevertheless, the exhaust half plays a more significant role with respect to the proportion of the total inducted charge and to the intensity of main coherent flow motion inside the combustion chamber, than the intake half does.

Table 4 compares the volumetric efficiency, λ_V , resulting from the five cases. Incorporating injection process with various timings leads to different λ_V than the premixed case, which is the direct consequence of discrepancies in mass flow rate. Specifically, mass flow rates of the injection cases are on average lower than that of the premixed case during the critical phase of intake when the valve lift is around the maximum (see Figure 14), owing to the coincident second-stage induction of fuel-rich charge. The high-volume flow rate window of intake phase for the injection cases is occupied by charges with lower-than-stoichiometric-mixture density. This is a feature peculiar to gas-fueled engines since the gaseous fuels often have low densities, whereas the admission of liquid fuel coincident with the maximum lift window may actually increase λ_V .

Case	Injection case				Premixed
	150	270	360	420	
λ_V	0.4253	0.4260	0.4370	0.4315	0.4351
$\Delta\%$	-2.3	-2.1	0.4	-0.8	0

Table 4 Comparison of volumetric efficiency

No general monotonic correlation is found between λ_V and EOI, as a result of complications caused by the two-stage mixing and fuel traveling. The air induction intervening between the first and second stage for case EOI 420 partly compensates the loss in flow density during the maximum intake window, and thereby its λ_V is negligibly impaired. The flow rate of case EOI 360 is not as much lower than the premixed case as case EOI 150 and 360 are. Together with constantly higher mass flow rate during the first-stage induction of leaner-than-premixed mixture, the resultant λ_V is marginally augmented above the premixed case. Reduction in λ_V is slightly more evident for case EOI 150 and 270. Given the similarity among case EOI 150, 270 and 360 in that all have significant second-stage induction and fuel stalling in the intake ports, it is inferred that the λ_V would decrease in an asymptotically diminishing way with advanced injection from EOI 360 backwards, until fuel crossing unacceptably impairs operability.

Moreover, since case EOI 270 is experimentally confirmed as the optimum injection timing, the decrease of 2.1% in λ_V and consequent total energy content may lead to discrepancies in the total amount of heat release with respect to experimental measurement, if the premixed case is instead used for numerical simulations. Specific to this case, the difference in λ_V alone is however not deemed significant but the implication is definitely worth taking into consideration.

Turbulence is another influential variable, and the underexpanded fuel jet is a well-established source of local turbulence due to the large-gradient shearing zones both embedded in and surrounding the jet core flow. To investigate the effects of injection or lack thereof, Figure 15 presents the turbulence kinetic energy both in the entire intake ports and in the vicinity of intake valves for the injection and premixed cases. Such distinction is made to explicate the extent to which the local turbulence effects of injection can be retained and transported downstream. Local increases in turbulence kinetic energy are comparable for all injection cases. The slightly lower turbulence created by later cases is expected, likely owing to the interference of intake flow imposing a nonnegligible ambient velocity that reduces local velocity gradients. The premixed case, devoid of injection, shows no sign of turbulence enhancement.

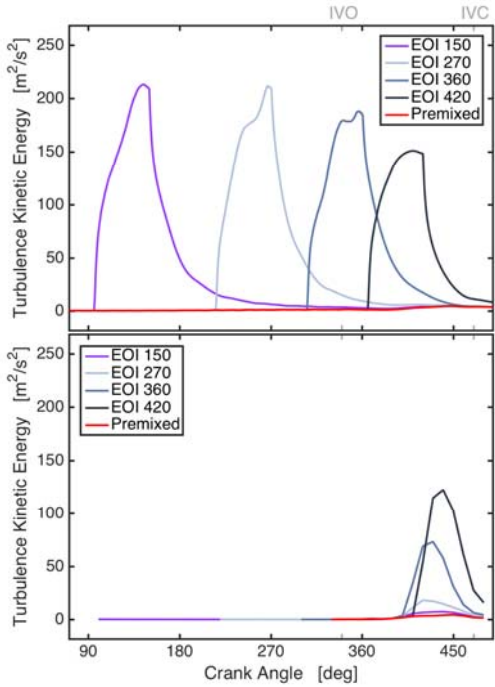


Figure 15 Turbulence kinetic energy in the intake ports (upper)
and upstream of the intake valves (lower)

However, due to finite fuel traveling speed and charge stalling at intake port branch, local increases in turbulence level in the vicinity of intake valves occur almost concurrently despite different EOIs. In addition, turbulence energy created by injection is dissipated to a greater extent for earlier injection, as a result of longer delay between injection event and charge arrival at intake valves. Accordingly, there appears to be a clear correlation that advancing EOI provides no benefits to the phasing of turbulence enhancement near intake valves but may instead lead to decrease in transported turbulence energy, with very early EOI granting little turbulence increase relative to no injection at all.

The eventual effects of turbulence enhancement by fuel injection inside the combustion chamber are presented in Figure 16 along with the coherent tumble motion, given the close connection between the two phenomena. The tumble motion, typical of and often purposely established in SI engines, is quantified by the dimensionless tumble number in the vertical plane of symmetry (xz-plane in the present work). The tumble number is essentially the normalized mass-weighted magnitude of total planar rotation, defined as

$$tumble\ number = - \frac{\sum m_i [w_i(x_i - X_V) - u_i(z_i - Z_V)]}{\frac{2\pi N}{60} \sum m_i [(x_i - X_V)^2 + (z_i - Z_V)^2]} \quad (7)$$

where m_i is the mass of cell i , x_i and z_i the coordinates of cell i , u_i and w_i the x and z-component of velocity of cell i , X_V and Z_V the coordinates of the instantaneous volume center of the combustion chamber, and N the engine speed in revolution per minute. Positive value denotes counterclockwise rotation in Figure 9 and 11.

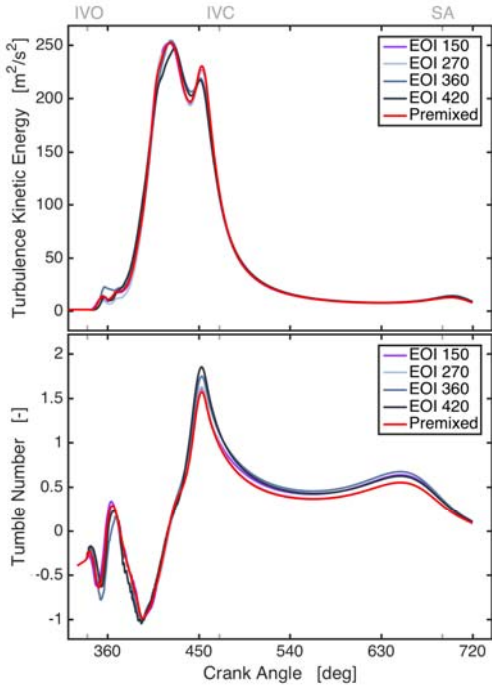


Figure 16 Turbulence kinetic energy and tumble number inside the combustion chamber

Initial oscillations in turbulence kinetic energy and tumble number appear upon IVO due to impulsive charge inflows and subsequent backflows. The principal phase of turbulence buildup and tumble establishment corresponds to the main charge induction, both the first and second-stage starting at ~ 370 degCA, wherein two peaks of turbulence are observed. The first peak occurs when the intake valves are at maximum lift with the highest mass flow rate in accord with Figure 14, after which the turbulence level declines as the intake flow diminishes towards IVC. The second peak occurs, coincident with the peak of tumble number, owing to intensification of the tumble motion in the mid-intake stroke when the piston movement is fast. Nevertheless, all the turbulence, built up either by high-velocity intake flow or by accelerated coherent tumble motion, is rapidly dissipated after IVC and further during the rest of the intake stroke. This tendency expectedly coincides with deceleration of the tumble motion.

Despite the correlation between local turbulence level near intake valves and EOI found in Figure 15, the intake-governed major turbulence enhancement phase shows little difference among all the cases. In particular, the premixed case has comparable turbulence buildup with the injection cases. The turbulence kinetic energy well preserved from injection site to intake valves for case EOI 420 grants no apparent advantages inside the combustion chamber. Rather, its relatively low intake mass flow rate during the second induction stage impairs turbulence production near the first turbulence peak at ~ 420 degCA, corresponding well to Figure 14. Accordingly, it is concluded that the direct effects of injection on in-cylinder turbulence level are insignificant regardless of the amount of injection-induced turbulence transported downstream to the back of intake valves. The upstream turbulence information is lost when the charge passes through the narrow valve openings at high velocity, and the turbulence buildup in this phase is more associated with intake mass flow rate.

Towards the spark advance, the superposed turbulence curves rise and diverge, following the reinforcement of tumble motion by the rapid upward piston movement during the compression stroke. The tumble motion is purposely established to enhance turbulence for combustion through the cascade transfer of kinetic energy, which is evidenced by the mismatch in time between the local tumble peak (at 650 degCA) and the turbulence

peak (at 700 degCA). The divergence of thus transferred turbulence level is supposed to stem from the differences in tumble intensity. Specifically, the tumble numbers of all the cases remain mostly identical in the main intake phase until shortly before IVC, implying that intake mass flow rate is not the major cause for the differing tumble intensities. A plausible explanation appears to be the relative spatial distribution of fuel and air in the combustion chamber. Given the much lower density of CH₄ than air, different distribution of fuel amounts to perceptibly different distribution of mass relative to the instantaneous center of tumble rotation. This speculation is substantiated by the remarkable agreement between the tumble numbers in Figure 16 and the CoV in Figure 10, in that, starting from 450 degCA (shortly before IVC), high tumble intensity corresponds to high mixture inhomogeneity. For instance, case EOI 420 initially has the highest CoV as well as the highest tumble number. The CoV then declines rapidly below the other cases, with its tumble number following the same trend. For the premixed case with perfect homogeneity, its tumble number is indeed expected to stay below all the injection cases.

Based on the proposed correlation between mixture inhomogeneity and tumble intensity, the tumble-associated turbulence production is supposed to intrinsically differ for all the cases. Nevertheless, energy transfer from mean-flow to turbulent motion and turbulence dissipation are complicated phenomena, especially towards the end of the compression stroke wherein the vortical tumble structure is confined by irregular geometries and deformed. The turbulence kinetic energy hence may not follow exactly the same trend as tumble number. To put things into perspective, turbulence kinetic energy at 700 degCA is reported in Table 4. The differences at the crank angle relevant to combustion may be regarded nonnegligible, considering the profound influences of turbulence on flame propagation.

Case	Injection case				Premixed
	150	270	360	420	
TKE	13.09	12.42	14.06	13.24	12.11
Δ%	8.1	2.6	16.1	9.3	0

Table 5 Comparison of turbulence kinetic energy (TKE, in m²/s²) at spark timing

As a final remark, it has to be pointed out that the results might be influenced by the specific turbulence modeling approach. As stated in the Numerical Method section, many references have suggested that turbulence models within the RANS k-epsilon family have very limited impact on the results. Even though LES is supposed to be more accurate than RANS, as it was reported in the Numerical Method section, the LES simulation of supersonic gas jets is really challenging, given the very wide range of turbulent scales involved. However, RANS simulations are still meaningful as can provide the relative assessment of different results, all with the same RANS turbulence model.

4.6 Experimental and numerical uncertainty

The results presented in this paper are affected by uncertainties given by measurement errors, modeling assumptions and numerical errors. The experimental data directly or indirectly referred to in this paper are: the main performance data used for the GT-Power model calibration, the in-cylinder pressure for the combustion model calibration in Ref. [50], and the air-fuel ratio. Based on previous works [71], the uncertainty of the in-cylinder measurements can be estimated within 2%. Considering the accuracy of the gas analyzers of 1%, the torque uncertainty of 0.3%, the expanded combined uncertainties of brake-specific emissions and air-fuel ratio are in the order of 2%–4%.

With reference to the simulation results reported in this paper, the main uncertainty are connected with the numerical-diffusivity-induced error in the quantification of the tumble number, the turbulence intensity, and the local air-fuel ratio. This uncertainty is closely connected to the size of the adopted mesh, and it is greatly reduced through the adoption of the high-order MARS discretization scheme. Furthermore, the grid effects on the tumble number and turbulence intensity have been minimized through the grid independence analysis performed in [51]. As far as the detailed prediction of the injection plume and local fuel concentration is concerned, the previously discussed mesh dependence analysis showed a marginal grid effect on the jet Mach number pattern, however, this has virtually no effect on the mixture stratification in the combustion chamber.

5 Conclusion

The gas fuel injection and air-fuel mixing process in a PISI CNG engine has been characterized. A method for modeling the injector and the engine as a whole has been developed as a diagnostic tool to identify the underlying mechanisms that have led to the observed experimental results referred to as a baseline.

- An injector model with the source cell approach has been developed. The source cell approach has the convenience of prescribing directly the fuel mass flow rate rather than inlet pressure boundary, and omits the injector inner flow passage by introducing proper source terms into the governing equations for a cluster of finite-volume cells near the injector nozzle. This model is able to capture shock structures typical of highly underexpanded jets that are of practical interest for the pressure ratio range of engine fuel injection applications.
- The modeling method is further generalized in regard to the insensitivity of source cell location and to the grid dependence of local refinement. It has been found that differences in describing the minor shock structures downstream of the predominant first shock cell and Mach disk have virtually negligible influences on fuel jet structure and mixing process in the combustion chamber. Whether such differences are due to source cell location or downstream grid refinement is irrelevant, provided that a reasonable spatial resolution not disrupting the minor shock waves is used. Covering the Mach disk with the same cell size as in the nozzle section and the rest of the supersonic core with double the size has proven suitable for investigating air-fuel mixing.
- There appears to be a threshold for PI timing, earlier than which the injected fuel is drawn back to the intake manifold, and the consequent inter-cylinder fuel crossing is responsible for the experimentally observed abnormal combustion, which is due to the unbalance of the A/F ratio between the cylinders.
- The two-stage mixing process has been revealed as a fundamental mechanism peculiar to PI gas engines. The first-stage induction of residual fuel from the previous cycle and the second-stage induction of fuel injected in the current cycle, as well as the proportion of fuel involved in the two stages, profoundly affect the mixing rate and fuel spatial distribution inside the combustion chamber.
- Restricted by local sonic speed and low density, momentum of the fuel jet is relatively low. The injected fuel hence travels at a limited speed and arrives from the injection site to intake valves with a noticeable delay. Fuel traveling along the intake ports is found to be determined by the relative timing between injection and IVO. Prior to IVO, the fuel travel distance is proportional to time as the ongoing injection is the propelling force. During the intake phase, the piston movement acts as the main driving force and fuel penetration scales with degCA. In the case of very early injection such that the fuel arrives at the intake port

814 branch before IVO, fuel penetration stalls only to resume after IVO. The fuel stagnation is a peculiar
815 feature of gas engines, negating fuel penetration benefit of further advancing the injection.

- 816 • The otherwise intuitive correlation between mixture homogeneity and EOI, i.e. earlier injection most likely
817 leads to better air-fuel mixing, is notably complicated by the two-stage mixing mechanism and fuel
818 traveling delay. Variation in EOI leads to two counterbalancing effects, the first being better premixing
819 attained with earlier EOI, and the second being more evenly split fuel mass between the two mixing states
820 with more postponed EOI. The respective inducted quantity of residual and freshly injected fuel is
821 determined by the relative timing between intake phase and fuel arrival, and the latter in turn depends on
822 the relative timing between injection and intake valve lift profile.
- 823 • By comparing different EOI cases with a premixed case, it has been argued that incorporating injection into
824 the numerical analysis of PI engines provides additional pertinent information. EOI has been found to affect
825 the intake mass flow rate as a result of local variation in fuel concentration and hence charge density. The
826 differences are most pronounced during the high-valve lift intake period and more so for the exhaust-side
827 half of the intake valve opening section. Volumetric efficiency is thereby directly influenced. Although
828 turbulence created by injection is locally comparable, the turbulence transported downstream to intake
829 valves has been found to decrease with advanced EOI. The initial buildup of in-cylinder turbulence
830 however appears to be insignificantly affected by turbulence upstream of intake valves, but rather
831 dependent on the high-velocity intake flow.
- 832 • A clear correlation between the coherent mean-flow tumble motion and mixture inhomogeneity has been
833 revealed. The mechanism seems associated with the spatial distribution of fuel mass fraction relative to the
834 instantaneous center of rotation. Therefore, turbulence enhancement close to combustion onset, through
835 cascade kinetic energy transfer, is intrinsically influenced by injection in an indirect way. The differences
836 in turbulence and the other abovementioned parameters caused by varying EOI may be considered
837 nonnegligible, or may alternatively provide insights into the interpretation of discrepancies between
838 numerical and experimental results.

839

840 Acknowledgement

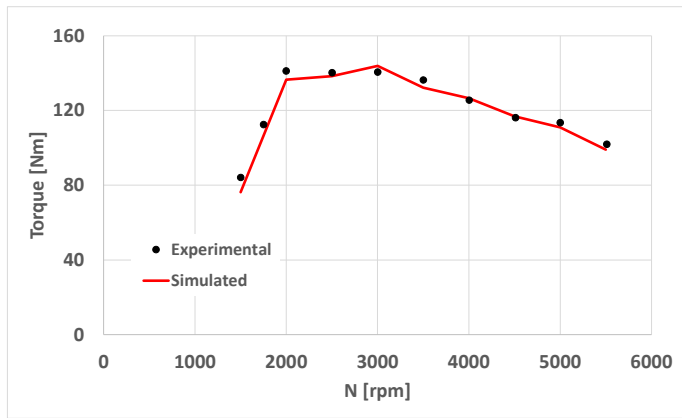
841 Financial support to this activity has been provided within the Biomethair regional research project
842 (Automotive platform of Regione Piemonte, Italy). The authors warmly thank Giorgio Carpegna, Andrea
843 Gerini, Francesco Perna, Andrea Stroppiana of Centro Ricerche Fiat S.C.p.A. for their valuable support.

844

845 Appendix: models validation

846 In this appendix the validation of the GT-Power model is provided, and a summary of the validation of the
847 CFD model (fully documented in [50] and [51]) is reported.

848 As mentioned in the paper, a GT-Power model was used to provide the high-frequency pressure boundary
849 conditions to the CFD model. Furthermore, the model was applied to a preliminary simulation of the effect of
850 injection timing on the cylinder-resolved A/F ratio, related to any differences of fuel and air trapped mass,
851 which might occur in the engine. The results of the validation of the GT-Power model are showed in Figures
852 A.1 and A.2.

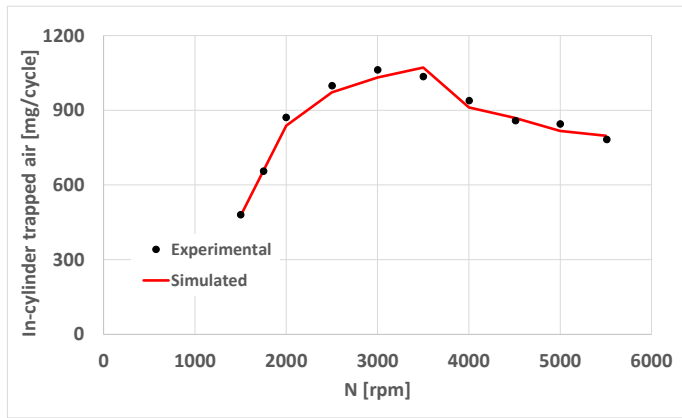


854

855 Figure A.1 GT-Power model validation: experimental vs. simulated engine torque.

856

857



858

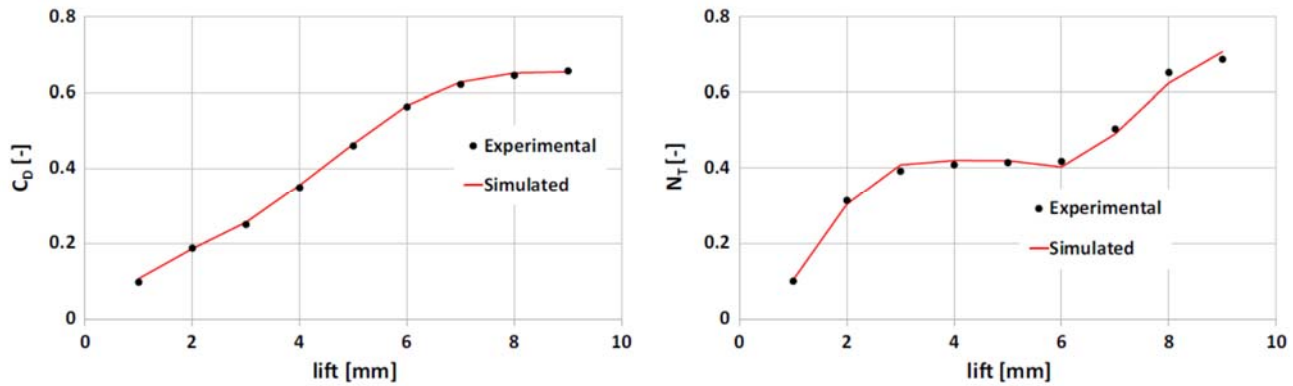
859 Figure A.2 GT-Power model validation: experimental vs. simulated air trapped mass.

860

861 As can be inferred from the charts, the model fairly reproduces the trends and the absolute values of the
 862 experimental engine, the differences being within 2-4%. The accuracy in the predicted air trapped mass is
 863 particularly significant for the purpose of the present paper, as it demonstrates the accuracy of the model in the
 864 description of the pressure waves in the intake and exhaust systems, as well as their effects on the trapped
 865 mass and A/F prediction.

866 The CFD model was extensively validated in previous papers from the same research group. More
 867 specifically, with reference to the description of the steady-state behavior of intake valve and port, Fig. A.3 is
 868 herein included, with the comparison of the flow coefficient and tumble number, which were already
 869 presented in [51]. The dependence of these parameters is well reproduced by the model, supporting its
 870 reliability in the reproducing the effects of different geometries and design solutions, such as those presented
 871 in this paper. Similar conclusions can be drawn from the in-cylinder pressure and heat-release comparison
 872 presented in [50], and included in this Appendix.

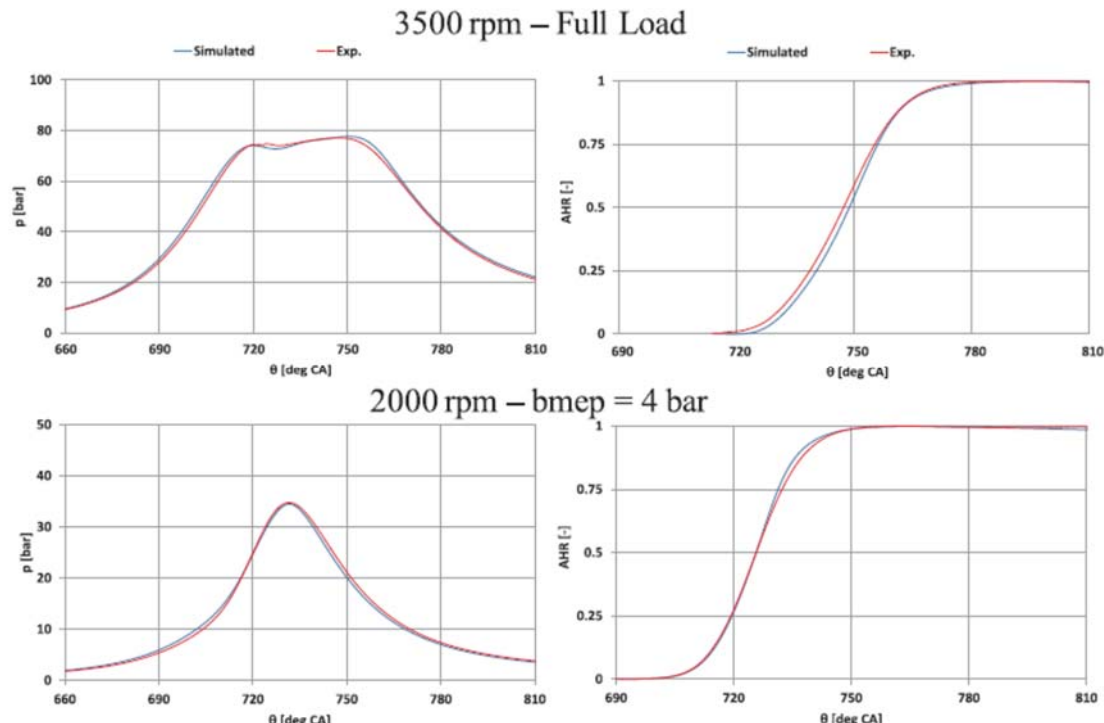
873



874

875 **Figure A.3** CFD model validation: experimental vs. simulated flow coefficients (left) and tumble number (right) against valve lift (taken from
876 [51]).

877



878

879 **Figure A.4** CFD model validation: experimental vs. simulated in-cylinder pressure and heat release, under premixed conditions (taken from [50]).

880

881

References

- [1] Exxon Mobil. Outlook for energy: A perspective to 2040. 2019, p.13-7.
- [2] IEA. CO₂ emissions from fuel combustion 2019. Paris: OECD Publishing, 2019. ISBN 9789264320215
- [3] Colvile RN, Hutchinson EJ, Mindell JS and Warren RF. The transport sector as a source of air pollution. *Atmos Environ* 35(9):1537-65, 2001.
- [4] OPEC. 2019 World oil outlook. OPEC, 2019, p.93-105. ISBN 9783950393682
- [5] Bae C and Kim J. Alternative fuels for internal combustion engines. *Proc Combust Inst* 36(3):3389-413, 2017.
- [6] Geng P, Cao E, Tan Q and Wei L. Effects of alternative fuels on the combustion characteristics and emission products from diesel engines: A review. *Renew Sust Energy Rev* 71:523-34, 2017.
- [7] Khan MI, Yasmin T and Shakoor A. Technical overview of compressed natural gas (CNG) as a transportation fuel. *Renew Sust Energy Rev* 51:785-97, 2015.

- [8] Kalghatgi GT. Developments in internal combustion engines and implications for combustion science and future transport fuels. *Proc Combust Inst* 35(1):101-15, 2015.
- [9] Korakianitis T, Namasivayam AM and Crookes RJ. Natural-gas fueled spark-ignition (SI) and compression-ignition (CI) engine performance and emissions. *Prog Energy Combust Sci* 37(1):89-112, 2011.
- [10] Cho HM and He BQ. Spark ignition natural gas engines – A review. *Energy Convers Manag* 48(2):608-18, 2007.
- [11] Thiruvengadam A, Besch M, Padmanaban V, Pradhan S et al. Natural gas vehicles in heavy-duty transportation – A review. *Energy Policy* 122:253-9, 2018.
- [12] Hu E, Li X, Meng X, Chen Y et al. Laminar flame speeds and ignition delay times of methane-air mixtures at elevated temperatures and pressures. *Fuel* 158:1-10, 2015.
- [13] El Merhubi H, Kéromnès A, Catalano G, Lefort B et al. A high pressure experimental and numerical study of methane ignition. *Fuel* 177:164-72, 2016.
- [14] Su J, Xu M, Li T, Gao Y et al. Combined effects of cooled EGR and a higher geometric compression ratio on thermal efficiency improvement of a downsized boosted spark-ignition direct-injection engine. *Energy Convers Manag* 78:65-73, 2014.
- [15] IEA. World energy outlook 2017. OECD/IEA, 2017. ISBN 9789264282308
- [16] Erfan I, Chitsaz I, Ziabasharagh M, Hajalimohammadi A et al. Injection characteristics of gaseous jet injected by a single-hole nozzle direct injector. *Fuel* 160:24-34, 2015.
- [17] Song J, Choi M and Park S. Comparisons of the volumetric efficiency and combustion characteristics between CNG-DI and CNG-PFI engines. *Appl Therm Eng* 121:595-603, 2017.
- [18] Moon S. Potential of direct-injection for the improvement of homogeneous-charge combustion in spark-ignition natural gas engines. *Appl Therm Eng* 136:41-8, 2018.
- [19] Yeh S. An empirical analysis on the adoption of alternative fuel vehicles: The case of natural gas vehicles. *Energy Policy* 35(11):5865-75, 2007.
- [20] Jahirul MI, Masjuki HH, Saidur R, Kalam MA et al. Comparative engine performance and emission analysis of CNG and gasoline in a retrofitted car engine. *Appl Therm Eng* 30(14-15):2219-26, 2010.
- [21] Pourkhesalian AM, Shamekhi AH and Salimi F. Alternative fuel and gasoline in a SI engine: A comparative study of performance and emissions characteristics. *Fuel* 89(5):1056-63, 2010.
- [22] Zhang CH, Xie YL, Wang FS, Ma ZY et al. Emission comparison of light-duty in-use flexible-fuel vehicles fuelled with gasoline and compressed natural gas based on the ECE 15 driving cycle. *Proc Inst Mech Eng D: J Automob Eng* 225(1):90-8, 2011.
- [23] Yao Z, Cao X, Shen X, Zhang Y et al. On-road emission characteristics of CNG-fueled bi-fuel taxis. *Atmos Environ* 94:198-204, 2014.
- [24] Adlercreutz L, Cronhjort A, Andersen J and Ogink R. Optimizing the natural gas engine for CO₂ reduction. SAE Technical Paper 2016-01-0875, 2016.
- [25] Zhang S, Wu Y, Liu H, Huang R et al. Real-world fuel consumption and CO₂ emissions of urban public buses in Beijing. *Appl Energy* 113:1645-55, 2014.
- [26] Thiruvengadam A, Besch M, Carder D, Oshinuga A et al. Unregulated greenhouse gas and ammonia emissions from current technology heavy-duty vehicles. *J Air Waste Manag Assoc* 66(11):1045-60, 2016.
- [27] Li W, Liu Z, Wang Z and Xu Y. Experimental investigation of thermal and diluent effects of EGR components on combustion and NO_x emissions of a turbocharged natural gas SI engine. *Energy Convers Manag* 88:1041-50, 2014.
- [28] Oh C and Cha G. Impact of fuel, injection type and after-treatment system on particulate emissions of light-duty vehicles using different fuels on FTP-75 and HWFET test cycles. *Int J Automot Technol* 16(6):895-901, 2015.
- [29] Donateo T, Tornese F and Laforgia D. Computer-aided conversion of an engine from diesel to methane. *Appl Energy* 108:8-23, 2013.
- [30] Liu J and Dumitrescu CE. Flame development analysis in a diesel optical engine converted to spark ignition natural gas operation. *Appl Energy* 230:1205-17, 2018.
- [31] Chandra R, Vijay VK, Subbarao PMV and Khura TK. Performance evaluation of a constant speed IC engine on CNG, methane enriched biogas and biogas. *Appl Energy* 88(11):3969-77, 2011.
- [32] Kobayashi K, Sako T, Sakaguchi Y, Morimoto S et al. Development of HCCI natural gas engines. *J Nat Gas Sci Eng* 3(5):651-6, 2011.
- [33] Fan B, Pan J, Yang W, Liu Y et al. Numerical investigation of the effect of injection strategy on mixture

948 formation and combustion process in a port injection natural gas rotary engine. *Energy Convers Manag*
949 133:511-23, 2017.

- 950 [34] Yan B, Wang H, Zheng Z, Qin Y et al. The effects of LIVC Miller cycle on the combustion characteristics
951 and thermal efficiency in a stoichiometric operation natural gas engine with EGR. *Appl Therm Eng*
952 122:439-50, 2017.
- 953 [35] Verma G, Prasad RK, Agarwal RA, Jain S et al. Experimental investigations of combustion, performance
954 and emission characteristics of a hydrogen enriched natural gas fuelled prototype spark ignition engine.
955 *Fuel* 178:209-17, 2016.
- 956 [36] Duan X, Liu Y, Liu J, Lai MC et al. Experimental and numerical investigation of the effects of low-pressure,
957 high-pressure and internal EGR configurations on the performance, combustion and emission
958 characteristics in a hydrogen-enriched heavy-duty lean-burn natural gas SI engine. *Energy Convers Manag*
959 195:1319-33, 2019.
- 960 [37] Yousefi A and Birouk M. Investigation of natural gas energy fraction and injection timing on the
961 performance and emissions of a dual-fuel engine with pre-combustion chamber under low engine load.
962 *Appl Energy* 189:492-505, 2017.
- 963 [38] Huang H, Zhu Z, Chen Y, Chen Y et al. Experimental and numerical study of multiple injection effects on
964 combustion and emission characteristics of natural gas-diesel dual-fuel engine. *Energy Convers Manag*
965 183:84-96, 2019.
- 966 [39] Yang B and Zeng K. Effects of natural gas injection timing and split pilot fuel injection strategy on the
967 combustion performance and emissions in a dual-fuel engine fueled with diesel and natural gas. *Energy
968 Convers Manag* 168:162-9, 2018.
- 969 [40] Movahed MM, Tabrizi HB and Mirsalim M. Experimental investigation of the concomitant injection of
970 gasoline and CNG in a turbocharged spark ignition engine. *Energy Convers Manag* 80:126-36, 2014.
- 971 [41] Singh E, Morganti K and Dibble R. Dual-fuel operation of gasoline and natural gas in a turbocharged
972 engine. *Fuel* 237:694-706, 2019.
- 973 [42] Mustafi NN, Raine RR and Verhelst S. Combustion and emissions characteristics of a dual fuel engine
974 operated on alternative gaseous fuels. *Fuel* 109:669-78, 2013.
- 975 [43] Ji C, Wang S and Zhang B. Performance of a hybrid hydrogen-gasoline engine under various operating
976 conditions. *Appl Energy* 97:584-9, 2012.
- 977 [44] Wang Y, Zhao Y, Xiao F and Li D. Combustion and emission characteristics of a diesel engine with DME
978 as port premixing fuel under different injection timing. *Energy Convers Manag* 77:52-60, 2014.
- 979 [45] Yang LP, Song EZ, Ding SL, Brown RJ et al. Analysis of the dynamic characteristics of combustion
980 instabilities in a pre-mixed lean-burn natural gas engine. *Appl Energy* 183:746-59, 2016.
- 981 [46] Ji S, Lan X, Cheng Y, Zhao X et al. Cyclic variation of large-bore multi point injection engine fuelled by
982 natural gas with different types of injection systems. *Appl Therm Eng* 102:1241-9, 2016.
- 983 [47] Rogers T, Petersen P, Koopmans L, Lappas P et al. Structural characteristics of hydrogen and compressed
984 natural gas fuel jets. *Int J Hydrg Energy* 40(3):1584-97, 2015.
- 985 [48] Dong Q, Li Y, Song E, Yao C et al. The characteristic analysis of high-pressure gas jets for natural gas
986 engine based on shock wave structure. *Energy Convers Manag* 149:26-38, 2017.
- 987 [49] Kakaee AH, Paykani A and Ghajar M. The influence of fuel composition on the combustion and emission
988 characteristics of natural gas fueled engines. *Renew Sust Energy Rev* 38:64-78, 2014.
- 989 [50] Baratta M, Misul D, Viglione L and Xu J. Combustion chamber design for a high-performance natural gas
990 engine: CFD modeling and experimental investigation. *Energy Convers Manag* 192:221-31, 2019.
- 991 [51] Baratta M, Misul D, Spessa E, Viglione L et al. Experimental and numerical approaches for the
992 quantification of tumble intensity in high-performance SI engines. *Energy Convers Manag* 138:435-51,
993 2017.
- 994 [52] Baratta M, Misul D, Xu J, Fuerhapter A et al. Development of a high performance natural gas engine with
995 direct gas injection and variable valve actuation. *SAE Int J Engines* 10(5):2535-51, 2017.
- 996 [53] Yan B, Tong L, Wang H, Zheng Z et al. Experimental and numerical investigation of the effects of
997 combustion chamber reentrant level on combustion characteristics and thermal efficiency of stoichiometric
998 operation natural gas engine with EGR. *Appl Therm Eng* 123:1473-83, 2017.
- 999 [54] Park H, Shim E and Bae C. Expansion of low-load operating range by mixture stratification in a natural
1000 gas-diesel dual-fuel premixed charge compression ignition engine. *Energy Convers Manag* 194:186-198,
1001 2019.
- 1002 [55] Baratta M, Catania AE and Pesce FC. Multidimensional Modeling of Natural Gas Jet and Mixture

- 1003 [Formation in Direct Injection Spark Ignition Engines – Development and Validation of a Virtual Injector](#)
1004 [Model. J Fluids Eng 133\(4\):041304, 2011.](#)
- 1005 [56] [Shu J, Fu J, Liu J, Ma Y et al. Effects of injector spray angle on combustion and emissions characteristics](#)
1006 [of a natural gas \(NG\)-diesel dual fuel engine based on CFD coupled with reduced chemical kinetic model.](#)
1007 [Appl Energy 233-234:182-95, 2019.](#)
- 1008 [57] [Keskinen K, Kaario O, Nuutinen M, Vuorinen V et al. Mixture formation in a direct injection gas engine:](#)
1009 [Numerical study on nozzle type, injection pressure and injection timing effects. Energy 94:542-56, 2016.](#)
- 1010 [58] [Baratta M and Rapetto N. Fluid-dynamic and numerical aspects in the simulation of direct CNG injection](#)
1011 [in spark-ignition engines. Comput Fluids 103:215-33, 2014.](#)
- 1012 [59] [Bartolucci L, Scarcelli R, Wallner T, Swanteck A et al. CFD and X-ray analysis of gaseous direct injection](#)
1013 [from an outward opening injector. SAE Technical Paper 2016-01-0850, 2016.](#)
- 1014 [60] [Deshmukh A, Vishwanathan G, Bode M, Pitsch H et al. Characterization of hollow cone gas jets in the](#)
1015 [context of direct gas injection in internal combustion engines. SAE Int J Fuels Lubr 11\(4\):353-77, 2018.](#)
- 1016 [61] [Scarcelli, R., Richards, K., Pomraning, E., Senecal, P.K. et al., “Cycle-to-Cycle Variations in Multi-Cycle](#)
1017 [Engine RANS Simulations,” SAE Technical Paper 2016-01-0593, 2016, doi:10.4271/2016-01-0593.](#)
- 1018 [62] [Baratta M, Chiriches S, Goel P, Misul D. “CFD modeling of natural gas combustion in IC engines under](#)
1019 [different EGR dilution and H₂-doping conditions”. Transportation Engineering, Vol. 2, 2020, 100018.](#)
- 1020 [63] [Shapiro, A.H., “The Dynamics and Thermodynamics of Compressible Fluid Flow”, Ronald, New York,](#)
1021 [1954.](#)
- 1022 [64] [Franquet E, Perrier V, Gibout S and Bruel P. Free underexpanded jets in a quiescent medium: A review.](#)
1023 [Prog Aerosp Sci 77:25-53, 2015.](#)
- 1024 [65] [Li Y, Kirkpatrick A, Mitchell C and Willson B. Characteristic and computational fluid dynamics modeling](#)
1025 [of high-pressure gas jet injection. J Eng Gas Turbines Power 126\(1\):192-7, 2004.](#)
- 1026 [66] [Yadollahi B and Boroomand M. The effect of combustion chamber geometry on injection and mixture](#)
1027 [preparation in a CNG direct injection SI engine. Fuel 107:52-62, 2013.](#)
- 1028 [67] [Crist S, Sherman PM and Glass DR. Study of the highly underexpanded sonic jet. AIAA J 4\(1\):68-71, 1966.](#)
- 1029 [68] [Ashkenas H and Sherman FS. The structure and utilization of supersonic free jets in low density wind](#)
1030 [tunnels. In: de Leeuw JH, editor. Proceedings of the 4th International Symposium on Rarefied Gas](#)
1031 [Dynamics 2\(7\). New York: Academic Press, 1965, p.84-105.](#)
- 1032 [69] [Maté B, Graur IA, Elizarova T, Chirokov I et al. Experimental and numerical investigation of an](#)
1033 [axisymmetric supersonic jet. J Fluid Mech 426:177-97, 2001.](#)
- 1034 [70] [Velikorodny A and Kudriakov S. Numerical study of the near-field of highly underexpanded turbulent gas](#)
1035 [jets. Int J Hydrot Energy 37\(22\):17390-9, 2012.](#)
- 1036 [71] [Baratta M, D'Ambrosio S, Misul D and Spessa E. Effects of H₂ addition to compressed natural gas blends](#)
1037 [on cycle-to-cycle and cylinder-to-cylinder combustion variation in a spark-ignition engine. J Eng Gas](#)
1038 [Turbines Power 136\(5\), 051502, 2014.](#)